DEVELOPMENT OF A FE BOLTZMANN TEMPERATURE LIDAR

By

Justin Breese

Recommended:

Advisory Comittee Chair

Department Head

Approved:

Dean, College Science, Engineering & Mathematics

Dean of the Graduate School

8-15-01

Date

DEVELOPMENT OF A FE BOLTZMANN TEMPERATURE LIDAR

A

Thesis

Presented to the Faculty

Of the University of Alaska Fairbanks

In Partial Fulfillment of the Requirements

For the Degree of

Master of Science

By

Justin Breese, B.S.

Fairbanks, Alaska

August 2001

Abstract

An iron Boltzmann temperature lidar allows the measurement of temperatures and iron densities in the mesopause region (~80-100 km). This thesis describes the initial development of a new Boltzmann temperature lidar at Poker Flat Research Range. An excimer-pumped dye laser system was installed in April 1999. During 1999 and 2000 this system was calibrated against the resident sodium system. Observations of iron were made in the winter of 2000 and spring of 2001. Temperature measurements were made in December of 2000. The thesis presents an operational analysis of the lidar system performance and a scientific analysis of the data obtained. The midwinter temperature measurements indicate the mesopause is above the mesospheric iron layer at this high-latitude site. The new lidar is an important development as it can be combined with Rayleigh lidar measurements to provide direct temperature profile soundings over the 30 to 90 km altitude range.

Table of Contents

List of Figures

List of Table

Acknowledgements

I wish to thank Dr. Richard Collins for providing me with a graduate position at the University of Alaska, Fairbanks and for his great amount of assistance as my advisor. I also appreciated the assistance, and helpful comments of my committee members William Simpson and Richard Benner. I would like to thank Keith Nowicki and Laura Cutler for their time in making the measurements used in the development of the iron lidar. Finally, I would like to acknowledge the support and assistance of the staff of the Poker Flats Research Range.

Dedication

I'd like to dedicate this thesis to Rebecca Lynn King. Without her I lack the dedication to move forward, but with her I have the ability to accomplish anything.

Chapter 1: *Introduction*

1.1 The Middle Atmosphere

The middle atmosphere is generally taken as the region containing the stratosphere, mesosphere, and lower thermosphere (10-110 km) [Wayne, 1985; Brasseur and Solomon, 1984]. An important feature of the middle atmosphere is the ozone layer. Figure 1.1 shows the basic temperature profile of the atmosphere along with altitude ranges for some atmospheric phenomena. The ozone layer, which occurs between 20 and 60 km in altitude, absorbs harmful ultraviolet (UV) radiation from the sun and it is this absorption of UV radiation that defines the stratopause. The absorption of radiation by ozone at the stratopause (≈50 km) causes it to be the warmest region in the stratosphere. The high temperature at the stratopause causes there to be a temperature increase across the stratosphere with warm air above colder denser air. This temperature gradient makes the stratosphere a very stable region in the middle atmosphere, stratified into layers based on temperature. The principle source of movement in the stratosphere is through diffusion. Above the stratopause is the mesosphere. In the mesosphere the temperature decreases with height as it does in the

troposphere placing cold dense air above warm less dense air. This gradient causes the mesosphere to be less stable than the stratosphere and thus more prone to turbulent mixing. At the mesopause the temperature again begins to increase due to the effects of solar wind. The mesopause on average is the coldest region in the atmosphere.

Mixing, energy transfer and general circulation are important in the middle atmosphere. Mixing defines how anthropogenic species are dispersed through the middle atmosphere, and their residence lifetimes. An important research area is how anthropogenic halogens interact with the ozone layer [Solomon, 1999]. Halogen destruction of ozone is important to life on earth. Reaction mechanisms of ozone and sources of halogens are areas of active research in hopes that ozone destruction can be minimized. An important source of energy transfer in the middle atmosphere is through gravity waves [Andrews, Holton, and Leovy, 1987]. Gravity waves are buoyancy waves produced by winds in the lower atmosphere. Gravity waves propagate up through the atmosphere. As the density of the atmosphere decreases the amplitude of the individual gravity waves must increase to maintain constant wave parcel energy. Eventually the amplitude of the wave becomes too large and causes the wave to become unstable. Once the wave becomes unstable it 'breaks' in the atmosphere, releasing energy. Gravity wave propagation and breaking are a large and important

source of energy transfer across the middle atmosphere. Gravity wave breaking and the associated energy transfer is thought to contribute to the general circulation of the upper stratosphere and mesosphere since circulation is not explained solely by a radiative model [Thomas, 1991]. Without additional energy, probably from gravity waves, the winds in the upper middle atmosphere can not be explained.

Several important structures in the middle atmosphere are driven by circulation. Polar vortices that occur during the winter months, form cyclonic winds around the poles that trap air, and prevent air exchange across the edge of the vortex. In this trapped air reactions with ozone deplete the layer without any replenishment of the ozone layer from outside the vortex. The lack of exchange leads to ozone 'holes' or regions of the atmosphere with a significantly lower amount of ozone. Ozone holes are of interest to us because they cause elevated UV radiation on the surface of the earth.

Measurements of these aspects of circulation require measurements of winds and temperatures in the middle atmosphere. Measurements in the polar regions are also important because the seasonal variation is much larger than at lower latitudes. Understanding the seasonal variation due to changes in solar flux helps to design and force consistency on models of global circulation.

1.2 Meteoric Metal Layers

At approximately 90 km the earth's atmosphere is dense enough that meteors striking the earth begin to ablate. Ablation is the process where the meteorite is heated by friction to a temperature where it begins to sputter off single atoms of matter. It is the process of ablation that produces the bright meteor trails sometimes visible to the naked eye called shooting stars. The ablation of meteors results in an influx of matter at this altitude. The meteoric input is approximately 44 tons per day [Hughes 1978] and results in metals being deposited in the atmosphere. The metals in the atmosphere are eventually lost from the atmosphere to the earth's surface.

Between the heights of 70 and 120 km the atmospheric conditions are such that these metals can exist in the atomic state. It is uncommon for atoms to be in the atomic state in the atmosphere. Above this altitude range the atoms are ionized, and below this altitude range they react with other atoms and form molecular species. This altitude range where metals are in the atomic state coincides with the upper mesosphere and lower thermosphere.

Since in the upper mesosphere and lower thermosphere the atoms are present in the atomic state, lidar can be used to probe the metal layers present using resonance fluorescence of the atoms. In a resonance lidar

system a laser transmits the specific wavelength of light that corresponds to an electronic transition in the atom. The light can be absorbed by the atom through a shift to an excited state. After a short period of time the excited atom will relax back to the ground, or unexcited state, and releases a photon. This photon is the same as the absorbed photon and can be emitted in any direction (isotropically). So by using a laser tuned to resonate with an atomic metal, the metal layer can be excited and the glow of the layer as it re-emits photons and relaxes can be measured on the ground with a telescope receiver. The two critical components required for such a measurement are a tunable laser, meaning that it can be 'tuned' or adjusted to the right frequency of light (usually by tilting a prism or grating [e.g. Hecht, 1992]), and a telescope receiver system as a method of detecting the low light levels (i.e. single photons) received. The meteoric metal layers provide a shiny target for measuring the middle atmosphere. Shiny targets are those with a high backscatter cross section. Typically resonance interactions have a backscatter of approximately 10^{-16} m^2 as compared to Rayleigh scattering, which has a backscatter of approximately 10^{-32} m^2.

Making measurements of atomic metal layers with a lidar system can give important information about gravity waves, temperatures and winds in a region of the atmosphere that other methods have difficulty measuring. The atomic metal layers act like a dye in that they are easy to see and measure

with an instrument, and can trace the state of the local atmosphere, which is transparent to the lidar system. Measurements can be made at high resolution in both space and time, with measurements at spatial scales of 75 m and time scales of several minutes at Poker Flat Research Range (PFRR).

While there are many different metals present in meteoric debris, sodium (Na) has been studied most extensively. Na is relatively easy to measure with a lidar system. It has a large scattering cross sectional area and the Na D line is located at 589 nm [Wiese, 1969]. This wavelength is right in the middle of the emission spectrum of Rhodamine 590, a commonly used and easily handled laser dye. Since Na is so 'shiny' and the dye that produces the laser light pulses is simple to use, there has been a proliferation of sodium lidar data, including density and temperature measurements.

A metal that is much more common in meteoric debris is iron (Fe). Fe atoms are almost twenty times more abundant in meteors than Na, with Fe making up 11.5% by weight, and Na making up 0.6%. Fe has not been as extensively measured as Na however because it's scattering cross sectional area is an order of magnitude smaller than that of Na. Furthermore, the dyes that fluoresce at the Fe resonance line of 372 nm are difficult to excite, and require a more sophisticated apparatus to produce laser light. Fe may not scatter light as strongly as Na, but there is more Fe present in the mesosphere to measure. Also a variety of the features in the Na layer appear

more pronounced in the Fe layer. For example the seasonal variation in Na is much less than the seasonal variation in Fe [Kane et. al., 1992]. Na also has narrow sporadic high-density layers that appear quickly and are not well understood [Collins et. al., 1996]. These layers are small compared to the large sporadic layers that are seen in Fe [Bills et. al., 1990]. All of these reasons indicate that Fe would be an interesting metal to measure, and suggest that it is a more sensitive tracer of the aeronomy of the middle atmosphere.

1.3 Laser Radar Studies

A basic laser radar or lidar (light detection and ranging) system is shown in Figure 1.2. The system is composed of a laser that generates pulses of light. These pulses of light are transmitted into the atmosphere. The transmitted light is scattered by aerosols and clouds through Mie scattering, by the molecules of air through Rayleigh scattering, and by resonant interactions with molecules and atoms through resonance scattering. The light that is scattered back towards the lidar facility is collected with a telescope. The collected light is focused onto a photodetector and quantified. The receiving telescope system usually also

includes some collimating optics, and filters to limit the color of light such that it matches the color of laser light being used. Filtering in this manner reduces background light noise. A high-speed digital recorder stores the signal that is scattered and received as the laser pulse travels away from the site. The initial laser shot is detected and recorded. This starting time is then used as a reference to determine the difference between the starting time of the pulse and the time that scattered light from that pulse is detected at the receiver. The difference between the starting time of the pulse, and the received scattered light can be used to determine the range of the object scattering the light. The range (z_s) can be calculated by a standard time-of-flight equation,

$$z_s = (tc)/2 \qquad [1.1]$$

In this equation c is the speed of light, and t is the time difference between the start of the transmitted pulse, and the received signal. For example, light scattered by a molecule at a distance of 3 km would be detected 2 μs after the laser fired ($(2*3x10^3\ m)/(3x10^8\ m/s) = 2x10^{-6}\ s$). Scattering from a distance of 30 km would be detected 180 μs later, 200 μs after the laser was fired. Accordingly by recording when the laser fires and the time of the received signal the system can easily trace the lidar signal with distance. When a lidar is a zenith pointing system this distance directly corresponds to altitude.

Measurements in the middle atmosphere are difficult to make. Weather balloons reach to approximately 30 km so they can probe the lower edge of the middle atmosphere. Radars can measure high and low altitudes, but in the middle atmosphere there is very little water, ions or electrons, which form most of the backscatter for radar signals. Airglow is used to probe the region around 80 km but is limited to certain times during the day to make measurements. These techniques leave a large portion of the middle atmosphere unmeasured; lidar can make these measurements.

Lidar can make accurate measurements of atmospheric quantities over the range of the middle atmosphere. Rayleigh scatter lidars can be used to measure temperatures through density and thus measure winds, Mie scatter lidars can measure aerosols, and resonance lidars can measure specific molecular and atomic species and make temperature measurements through a variety of spectroscopic techniques. Lidars can also make important measurements on the time scales of interest, from minutes to years. The middle atmosphere is important to research and lidars provide an important method for measuring quantities in the middle atmosphere.

1.4 Lidar Studies at PFRR

A Na resonance lidar was installed at PFRR in the fall of 1994. The first measurements of the mesospheric Na layer at PFRR were made in November 1994 and measurements have continued on an ongoing basis since February 1995. This lidar system employs a flashlamp-pumped dye laser that was manufactured by the Candela Laser Corporation of Bedford, MA. The laser model is a Candela LFDL-1 (Linear Flashlamp Dye Laser model 1) and is a simple rugged laser system that has made campaign measurements in Illinois, Hawaii, Antarctica, and Alaska. The LFDL-1 has also been deployed in both airplanes and field stations. The LFDL-1 is a classic Littrow cavity [Silfvast, 1996] with a tunable grating and an inline single-slab etalon. The LFDL-1 is a broadband laser that requires continuous monitoring and adjustment during operation.

In 1997 a Rayleigh lidar was installed at PFRR as part of a collaborative relationship between the Communications Research Laboratory (CRL) and the Geophysical Institute of the University of Alaska, Fairbanks (GI-UAF). The Rayleigh lidar system employs a powerful solid-state Nd-YAG laser manufactured by the Continuum Laser Corporation of Santa Clara, CA. This laser is a Continuum model 8020. The lidar system uses Rayleigh scatter to profile the stratosphere and mesosphere. The data

from the Rayleigh lidar has been used to determine the temperature profile of the middle atmosphere from 40 to 80 km [Mizutani et. al., 2000; Cutler, 2000; Cutler et. al., 2001]. One limitation of Rayleigh lidar temperatures is that they require a seed temperature in the upper atmosphere, but with a seed temperature Rayleigh lidars are quite accurate.

The lidar signal obtained with the GI-UAF Na resonance lidar and the CRL Rayleigh lidar on the night of 14-15 November 1997 is plotted in Figure 1.3. The resonance lidar signal decays with altitude up to approximately 60 km. This signal is due to the Rayleigh scatter from the air. As the air density decreases with altitude so does the lidar signal. Between 70 and 110 km the resonance scattered signal from atomic Na is clearly visible. To create this resonance interaction the Na lidar operates at a wavelength of 589 nm. Light at 589 nm is yellow in color and resonantly couples with atomic Na. This resonant coupling is approximately 10^{16} times greater than Rayleigh scattering. The Rayleigh lidar signal also decreases with altitude like the Na system. However the solid-state laser in the Rayleigh system produces laser pulses that have larger energies than the dye laser so the lidar signal from the Rayleigh system at lower altitudes is larger. The solid-state laser also operates at a wavelength of 532 nm. Light at 532 nm is a green color and does not resonantly couple with atomic Na (or any other atomic metal). The lack of resonant coupling between the Rayleigh

laser light and the metal layer atoms renders those layers (≈90 km) invisible to the Rayleigh lidar system.

The goal of operating both resonance and Rayleigh lidar systems at PFRR is to yield concurrent measurements in the upper mesosphere and lower thermosphere with resonance lidar and mesosphere and upper stratosphere with Rayleigh lidar. These measurements support studies of the middle atmosphere from lower altitudes where waves and tides are generated to higher altitudes where these waves break and drive mean flow.

In 1999 GI-UAF acquired an excimer pumped dye laser system from the Lambda Physik Corporation of Fort Lauderdale, FL. This laser system consists of a Lambda Physik model LPX210i excimer laser coupled with a Lambda Physik model Scanmate 2 dye laser. The excimer laser is a XeCl laser and operates at a wavelength of 308 nm, which is ultraviolet (UV) light (Hecht, 1992). The light from the excimer laser is used to pump or excite the Scanmate 2 dye laser. This Lambda Physik laser system, built nearly 20 years later, is considerably more sophisticated than the Candela LFDL-1. The Scanmate 2 can operate with a wide variety of laser dyes and so can be used to measure a variety of atmospheric species (i.e. Na at 589 nm, Fe at 372 nm and 374 nm, and N_2^+ at 392 nm). Furthermore, the Scanmate 2 laser is engineered with a precision grating to allow changing the operating wavelength in 1pm steps. For comparison the LFDL-1 is limited to

measurements of Na because it is unable to pump the dye used for Fe, and is maintained at a single wavelength to maximize the signal from the Na layer. The Scanmate 2 generates laser light at a greater intensity and wavelength stability than the LFDL-1. These properties of the Scanmate 2 allow it to make better resonance lidar measurements.

1.5 The Goal and Scope of this Study

The goal of this thesis is to make temperature measurements of the mesosphere using a Fe Boltzmann temperature lidar. To achieve this goal three steps needed to be completed. First the Lambda Physik laser system had to be installed at PFRR, and integrated with the lidar receiver system. Then the performance of the new lidar had to be characterized with Na so that the new data could be compared with the previously collected data taken at the PFRR site. Lastly the lidar needed to be characterized with Fe so that the Fe Boltzmann temperature measurements could be made.

Bringing the new lidar system online and characterizing it with Na allows continuity with the past 6 years of measurements at PFRR. Getting a chance to use the higher resolution capabilities of the new lidar during the Leonids meteor shower would also add to the existing data-set at PFRR.

Having a large data-set spanning 6 years provides important information and is used to determine small trends such as the debated global warming trend.

Once the lidar system was characterized the next goal was to change the system over to UV operation and make measurements of the mesospheric Fe layer. Making regular measurements of Fe with Na will add to the quality of data collected in that two simultaneous measurements allow for uncertainty. An example of this uncertainty in measurements is the discovery of meteor trails in lidar measurements [Kane and Gardner, 1993]. Originally thought to be noise meteor trails measured at the same site simultaneously on two different systems revealed that the trails were real phenomena and not noise. Analysis of two simultaneous data-sets would greatly assist in current gravity wave research and provide another indicator of the state of the mesosphere. Having two simultaneous data-sets allow the determination of what environmental factors affect the metals.

The last goal was to make mesospheric temperature measurements with the Fe Boltzmann technique [Gelbwachs, 1994]. Showing this would highlight that with a relatively uncomplicated lidar system it is possible to make valuable measurements of mesospheric temperatures. To date there are very few lidar measurements of mesospheric temperature. These measurements would be critical in the analysis of the current Raleigh temperature lidar also at the site by providing the seed temperature needed

for the Rayleigh analysis. With Rayleigh and Fe Boltzmann factor lidars the PFRR site could provide valuable high latitude atmospheric temperature measurements from 30 to 90 km in altitude.

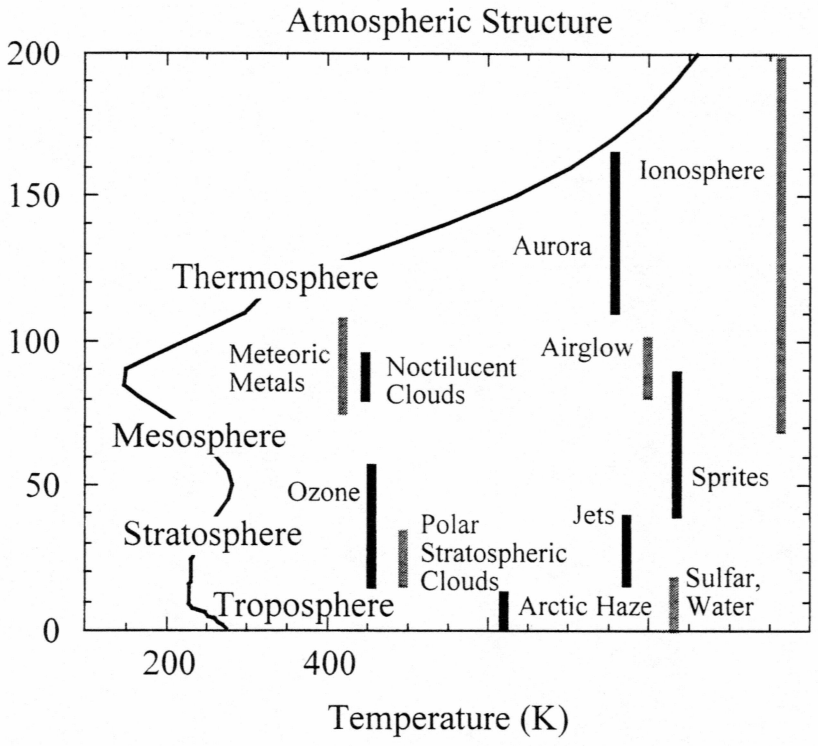

Figure 1.1: The temperature profile of the atmosphere and the height ranges of some interesting atmospheric phenomena

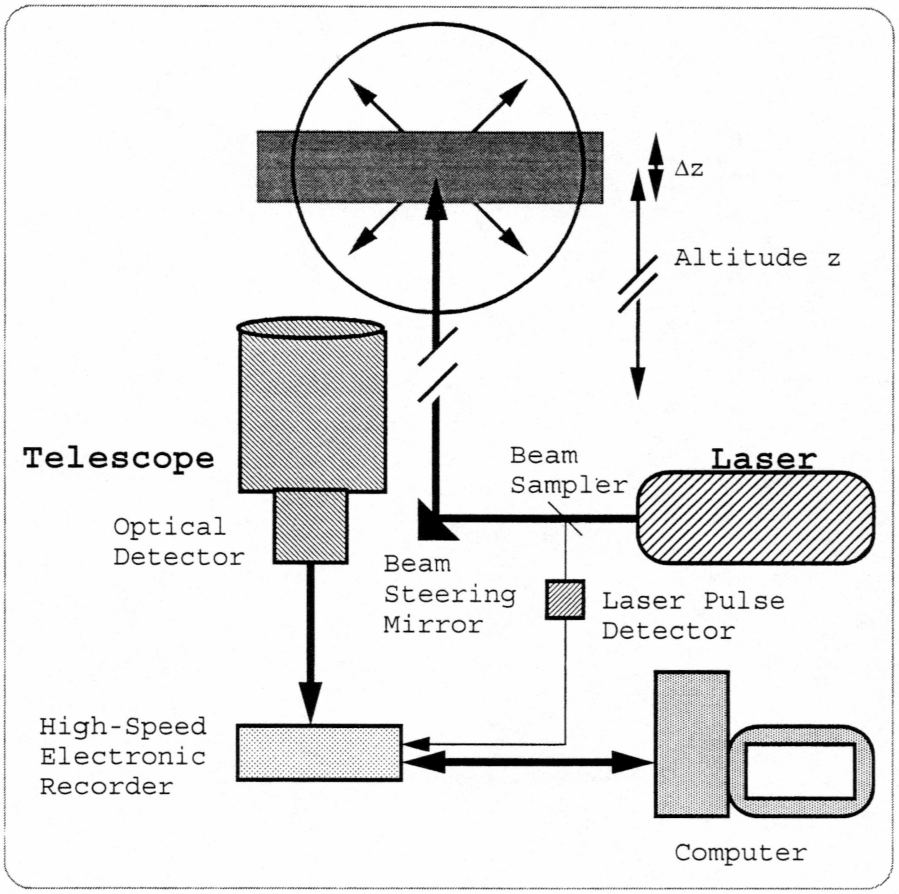

Figure 1.2: A diagram of a basic lidar system

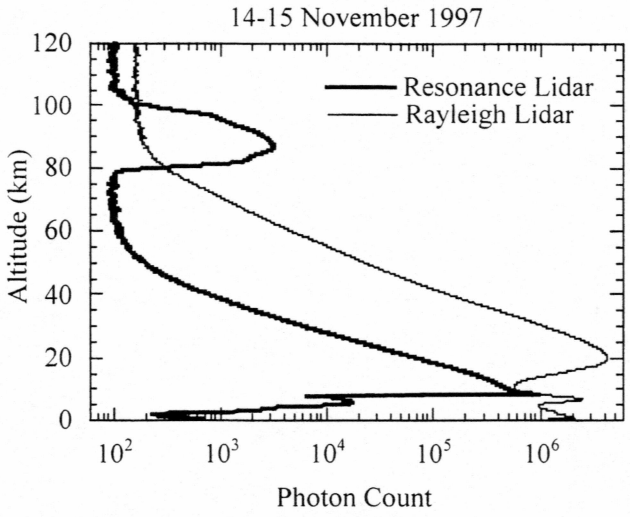

Figure 1.3: The lidar signal returns of a Rayleigh lidar and a resonance lidar

Chapter 2: *Spectroscopy*

2.1 Introduction

The alkali atoms (i.e. lithium (Li), sodium (Na), potassium (K), rubidium (Rb), and cesium (Cs)) like hydrogen are the prototypes for one-electron atomic electronic transitions [Herzberg, 1944; Atkins, 1991]. The atomic number determines the nuclear charge of atoms because it defines the number of protons in the nucleus. The nuclear charge then determines the number of electrons in the atom's electronic shell. The nuclear charge also determines how tightly bound electrons are. Atoms with high nuclear charge have orbitals that are compressed such that the electrons are restricted to space closer to the nucleus. Alkali atoms contain filled inner shells and have one valence electron. The observed spectral emissions are due to transitions by this single valence electron.

The smaller alkali metals (i.e. Li, Na, and K) have less complicated emission spectra than the larger atoms (i.e. Rb, Cs, and Fe). This difference in spectra between large and small atoms is due to the reduced nuclear charge. Reducing the nuclear charge reduces the effects of spin-orbit

coupling. In this chapter we give a brief overview of quantum mechanics as it applies to the fine and hyperfine structure of atoms.

2.2 The Fine Structure

The fine structure in atomic spectra arises from the splitting of energy levels due to spin-orbit coupling. The splitting is a result of an interaction between the magnetic field due to the orbital angular momentum denoted **l**, and the magnetic field due to the intrinsic spin of the electron denoted **s**. Orbital angular momentum is created by the electron's motion about the nucleus. The electron's motion represents a moving charge and thus is a current. This current induces a magnetic field. The spin angular momentum is much like this representing a spinning charge. Likewise the spinning charge represents a current which produces a magnetic field. Both **l** and **s** are vectors with quantized magnitudes as required by quantum mechanics. Each quantity has a corresponding quantum number l and s, which are required to have integer, or half integer values. The momentum vectors **l** and **s** couple vectorialy to give the total angular momentum vector, $\mathbf{j} = \mathbf{l} + \mathbf{s}$. Total angular momentum is also quantized and has corresponding quantum number j, again constrained to be integer or half integer in value. Coupling

spin and orbit momentum described by quantum numbers l and s leads to possible values of,

$$j = |l + s|, |l + s| - 1, \ldots, |l - s|. \qquad [2.1]$$

How these two magnetic fields interact, either in a positive manner or negatively, define the splitting due to spin-orbit coupling [Atkins, 1991].

Since this coupling is occurring in regards to a single electron, lower-case letters are used to indicate these are the momentum vectors and values for that electron. When these values are applied to the entire atom, then upper-case values are used. For the alkali atoms, there is only one valence electron so the electron momentum values are the values for the entire atom. In multi-valence electron atoms, the individual momenta of the electrons must be combined to determine the overall momentum of the atom.

As the size of the atom grows so does the splitting due to the spin-orbit coupling. If we take the orbital angular momentum as constant for an orbital, increasing the nuclear charge increases the speed of the electron when it is near the nucleus and thus also increases the associated magnetic field. In addition to this increase, as the nuclear charge increases the orbitals are compressed. The compression refers to a shrinking of the orbital size due to the increased attraction of the nucleus. Since the nuclear charge has increased, the electrons are constrained closer to the nucleus. Since the electrons are closer, they are exposed to higher magnetic fields. The energy

level splitting, based on the nuclear charge, increases proportional to z_N^4 where z_N is the nuclear charge [Atkins, 1991].

The effect of nuclear charge is seen in the fine structure splitting of Na and Fe. In Na there is no fine structure splitting of the ground state, but the fine structure splitting in the excited state is $\approx 27\ cm^{-1}$ [Wiese, et. al., 1969]. In comparison Fe fine structure splitting of the ground state and the first excited state is $\approx 416\ cm^{-1}$ [Fuhr, et. al., 1988]. It is the presence of fine structure splitting in the ground state and the magnitude of the splitting that causes there to be a population difference, that is dependant on temperature, between the two states [Atkins, 1994]. This population difference makes temperature measurements with the Boltzmann technique useful for Fe. In Na there is no separation of the ground state due to fine structure splitting.

2.3 Hyperfine Splitting

The hyperfine structure in atomic spectroscopy arises from an interaction between the magnetic field of the electron in a spin orbital and the magnetic field of the nucleus. Just like the coupled spin and orbital angular momentum, **J**, give the electrons an associated magnetic field, the nucleus also has angular momentum, **I**, and an associated magnetic field.

The vectors **J** and **I** couple vectorialy to give **F** = **J** + **I** where **F** is the total angular momentum including nuclear spin. Again F quantum number values are given by the Clebsch-Gordan series,

$$F = |J + I|, |J + I| - 1, \ldots, |J - I|. \qquad [2.2]$$

While the angular momentum of the nucleus is equivalent to the angular momentum of the electron the mass of the nucleus is much greater than the mass of the electron. This difference in mass means that to achieve an amount of angular momentum the nucleus does not need as much motion as the electron. The slower motion of the nucleus decreases the current caused by the motion of the charged nucleus and the decreased current reduces the corresponding magnetic field. The nuclear magnetic field is approximately 1000 times smaller than the field associated with an electron. Because the fields associated with the hyperfine structure are so small it is no surprise that the splitting of energy levels is also typically 2000 times smaller than the fine structure splitting [Atkins, 1991].

Electrons that come into direct contact with the nucleus, for example the s orbital electrons, can couple with the magnetic field of the nucleus through a Fermi contact interaction. The Fermi contact interaction can be viewed as a non-dipolar interaction. In this type of interaction the electron is so close to the nucleus that the nucleus no longer affects the electron as if they were both point charges. The nucleus in the Fermi contact interaction

is equivalent to a loop of current with the diameter of the nucleus. Only electrons that come into direct contact with the nucleus experience this kind of angular momentum coupling. This restriction is because only these electrons can be close enough to experience the nuclear force as anything other than a point charge.

While the Fermi contact interaction occurs most strongly with s electrons, other types of orbitals can also experience energy splitting due to nuclear interactions. The p orbitals can be split due to nuclear coupling because they are close enough to experience a dipole type coupling. The p orbital energy splitting is much smaller than the direct coupling of the s electrons through Fermi contact interaction. Orbitals farther away have interactions that result in negligible energy level splitting for Na and Fe [Atkins, 1991]. In both Fe and Na, the hyperfine splitting is not large enough to have energy level population differences due to temperature.

2.4 Spectroscopy of Sodium

Sodium (Na), with an atomic mass of 23 (^{23}Na), is the second lightest of the alkali earth metals. Na has two filled inner shells ($1s^2 2s^2 2p^6$) and one valence electron in the outer shell ($3s^1$) [Atkins, 1994; Cotton, 1967]. The

observed spectral emissions are due to transitions of Na's single valence electron between different electronic states. The transition observed by most lidar systems is the Na D line transition, which occurs at 589 nm and has an Einstein A coefficient of 0.63×10^8 Hz. The ease of handling gaseous Na in the laboratory and simple quantum mechanical description explain widespread use of Na in experimental studies of quantum mechanics [Demtröder, 1996].

Na has a single valence electron that occupies a 3s orbital when Na is in the ground state. Figure 2.1 shows the Grotrian diagram for Na. For a 3s electron L=0 and S=1/2 so J=1/2 and the term for the ground state is $^2S_{1/2}$. This ground state of Na is split into two levels by hyperfine interactions. The excited state for the D transition ($1s^2 2s^2 2p^6 3p^1$) places the 3s electron in the 3p orbit. For the excited state L=1 and S=1/2 so the J values are J=3/2 and J=1/2. There are therefore two terms in the excited state $^2P_{3/2}$ and $^2P_{1/2}$ due to spin orbit coupling or fine structure effects.

The hyperfine structure for sodium causes the $^2S_{1/2}$ state to split into two levels, the $^2P_{1/2}$ state to split into two levels and the $^2P_{3/2}$ state to split into four levels. Nuclear spin (I) for Na is 3/2 [Herzberg, 1944].
From the Clebsch-Gordan series there are either 2J+1 energy levels if J>I or 2I+1 energy levels if J<I. For the $^2S_{1/2}$ and $^2P_{1/2}$ states F = {2,1}, for $^2P_{3/2}$ state F = {3,2,1,0}. The separation of the ^2P states due to J leads to two

spectral lines that are transitions from $^2S_{1/2}$ to $^2P_{1/2}$ and $^2S_{1/2}$ to $^2P_{3/2}$. The separations of the D lines are labeled D_1 for the $^2S_{1/2}$ to $^2P_{1/2}$ transitions and D_2 for the $^2S_{1/2}$ to $^2P_{3/2}$ transitions. In the D_2 line there is further distinction in the labeling of the hyperfine structure of the transition lines. Transitions from $^2S_{1/2}(F=2)$ level to $^2P_{3/2}$ states are labeled D_{2a} and transitions from $^2S_{1/2}(F=1)$ level to $^2P_{3/2}$ states are labeled D_{2b}. This labeling of hyperfine lines occurs because the hyperfine splitting of the $^2S_{1/2}$ state is much larger than the hyperfine splitting in the $^2P_{3/2}$ state. The difference in the splitting magnitude of these two energy levels is due to the strong coupling of s electrons with nuclear angular momentum as compared to the weak coupling with p electrons.

There are six possible transitions in the Na D_2 spectral line because transitions from $^2S_{1/2}(F=1)$ to $^2P_{3/2}(F=3)$ and $^2S_{1/2}(F=2)$ to $^2P_{3/2}(F=0)$, require a change in J of 2, which is forbidden by selection rules. J can only change by 0 or ± 1. Using a central wavelength for the Na D_2 line of 589.15826 nm *in vacuo* [Fricke and von Zahn, 1994], the different frequency offsets, listed in Table 2.1, from this value give an idea of how small the splitting due to nuclear spin is.

Ideally the emissions associated with atomic transitions would be monochromatic with lines appearing as delta functions. However, due to the finite lifetime of the states there is a range of energies for each state, which

causes lifetime broadening to occur. Lifetime broadening gives a spread in frequency to the emission, and the shape of this spread in frequency is termed the lineshape. At 0 K the only broadening would be lifetime broadening of these lines. The lifetime broadening is given by,

$$\Delta\nu = A/(2\pi). \qquad [2.3]$$

Where A is the sum of Einstein A coefficients for transitions from the upper state and the lower state. Since the lower state is the ground state there are no transitions from it to a lower state (there is no state lower than the ground state) so only transitions from the upper state need to be addressed. The D transition is also the fundamental transition for Na, so the lifetime broadening can be closely approximated using the D transition only. For Na the lifetime broadening is ≈ 0.0003 cm^{-1}. This lifetime or natural broadening yields a lineshape that has a Lorentzian shape.

For any sample that is not at 0 K there will be some movement of the atoms. In a gaseous sample this leads to inhomogeneous broadening. In a gas, at some temperature T, each of the atoms present will be moving in a random direction at a specific speed. Different atoms will have different speeds and this speed distribution is called a Maxwell distribution. The fractional number of atoms, *f*, at a specific speed, *s,* in the gas will be given by,

$$f(s) = 4\pi \left[\frac{M}{2\pi RT} \right]^{3/2} s^2 e^{-\left(Ms^2 / 2RT \right)} \qquad [2.4]$$

where M is the particle mass in grams, R is the universal gas constant (8.31 J/(Kmol)), and T is the temperature in Kelvin [Atkins, 1994].

While the speed of the particles is given by the above equation, the direction of each is random. For a fixed observer some particles will be moving toward the observer, some will be moving away, and some will appear to be fixed by moving orthogonally to the observer's line of sight. For a particle moving away from a light source, the light appears to be at a longer wavelength. To particles moving toward the light source the wavelength appears shorter than the motionless case. This wavelength shift is the classic Doppler effect. Thus a monochromatic source appears to the population to have a distribution of wavelengths. Similarly, for a radiating gas, the observer sees a distribution of wavelengths rather than a monochromatic source. This broadening is termed inhomogeneous broadening as different populations of atoms contribute the different wavelength components. In this case the populations are defined by their velocity projection along the path of the laser. Inhomogeneous broadening can also arise from a gas where a population of isotopes is present. Because the speeds have a random distribution about zero, the line emission appears as a Gaussian function. Adding the presence of motion due to lifetime

broadening to the Doppler broadening yields a Voigt function. Near 200 K the Doppler effects broaden the lineshape much more than the lifetime broadening so a Gaussian shape is an accurate approximation for the lineshape [Verdeyen, 1981].

While Doppler broadening is not terribly large, the differences in energy of the hyperfine splitting of the sodium D_2 line are of similar magnitude. This similarity causes the lines to overlap even at modest temperatures usually so that there are only two lines discernable, the D_{2a} and the D_{2b} lines. The hyperfine line groups, D_{2a} and D_{2b}, are shown in Figure 2.1. The Doppler width at 200 K is 2 pm, while from Table 2.1 the splitting between the individual hyperfine structure levels is about 0.06 pm for the D_{2b} group of lines, and 0.11 pm for the D_{2a} group of lines, from Table 2.1. The splitting between the D_{2a} and D_{2b} lines is about 2 pm, which is the same as the Doppler width. Doppler broadening causes the small hyperfine splitting lines within the a and b branches to be completely obscured, and only the two main branches are discernable. At higher temperatures the Doppler width increases which begins to obscure even these two branches [Fricke and von Zahn, 1994].

2.5 Spectroscopy of Iron

Iron with an atomic mass of 56 (^{56}Fe), is in the middle of the transition elements of the periodic table. Iron has three filled inner shells ($1s^2 2s^2 2p^6 3s^2 3p^6$) and has eight valence electrons in its outer shell ($4s^2 3d^6$) [Atkins, 1994; Cotton, 1967]. Because the spectral lines of an atom are due to the transitions of valence electrons, Fe has a much richer spectrum than Na. The large number valence electrons and high nuclear charge of Fe atoms leads to a complicated quantum mechanical description. The complicated description of Fe means that currently numerical methods must be used to model Fe's structure. Using numerical methods means the spectra not absolutely determined due to approximation errors in numerical methods. With smaller atoms these errors are not to large but as the atoms get heavier these errors get larger. Because of approximation errors the values for the spectral lines of most atoms, and especially heavy atoms like Fe, are experimentally measured [Fuhr et. al., 1988].

The ground state of Fe is described by the term a^5D and several different transitions are possible from this state. The Grotrian diagram of Fe is shown in Figure 2.2. For a^5D, $S = 2$, $L = 2$, which yields $J = \{4,3,2,1,0\}$. For a^5D the ground state is a^5D_4, and the next state is a^5D_3 which is split by 415.9 cm^{-1}. Because the valence electrons in Fe reside in d orbitals the

hyperfine structure is negligibly small in Fe. The fine structure splitting in Fe however is much larger than that of Na. This magnitude is caused by the increased nuclear charge. In Fe the nuclear charge is twice the nuclear charge of Na. The ground state splitting in Fe is due to fine structure splitting, and has an energy of 488.1 cm^{-1} [Fuhr et. al., 1988]. In Na the ground state splitting is due to hyperfine splitting with splitting energy of 0.59 cm^{-1} [Fricke and von Zahn, 1994] for Na. The small splitting energy in the ground state of Na means there is not a large difference in populations of the split ground state. However, in Fe the splitting values are quite large and some of the energy levels in the ground state are virtually unpopulated.

The Fe ground state is split into five different states. The fraction of the total population that is in each state is calculated by using Boltzmann's equation for the population of a state,

$$\frac{N_i}{N_j} = \frac{g_i}{g_j} e^{-\left(\left(E_i - E_j\right)/kT\right)} \qquad [2.5]$$

where N_i is the population, g_i is the degeneracy, and E_i is the energy in state *i*, N_j is the population, g_j is the degeneracy, and E_j is the energy in state *j*, k is Boltzmann's constant (1.38×10^{-23} J/K), and T is the absolute temperature (K). From this we can see that to get optimal temperature sensitivity the change in energy needs to be close to the value of kT (139 cm^{-1} at 200 K).

At a typical mesospheric temperature of 200 K the ratio of the populations in such a system, assuming the states have equal degeneracies, is $N_0 \approx 3N_1$, where N_0 is the lower state, and N_1 is the upper state in the transition. For Fe at 200 K most of the atoms (≈96%) are in the lowest energy level, a small portion (≈4%) are in the first excited state, and a negligible amount of atoms in the rest of the states (<1%). The populations of the different a^5D states are shown in Table 2.2. In Na the populations are not temperature dependant due to the small splitting energy. The difference in energy for Fe is approximately 3.5 times larger than the amount desired for maximum sensitivity, whereas the difference for Na is 235 times smaller than the desired amount for maximum sensitivity.

The only two states in Fe that have appreciable populations are the ground state and first excited state. Transitions from these two states to the excited z^5F° state occur at 372 nm (actual value 371.993 nm) and 374 nm (actual value 373.713 nm). The separation of these two lines is 1.7nm. The transitions from the a^5D state to the z^5F^o state are all listed in Table 2.3. The Doppler width at mesospheric temperatures is slightly narrower than Na but still approximately 2pm. These lines are well separated. Even if the two lines were probed with a broad laser line (≈100pm) there would be no overlap. The population of these two states and thus their separation in

wavelength make Fe a good candidate for measuring temperatures by spectral techniques.

Table 2.1: Offsets for the sodium D_2 line due to hyperfine splitting.				
	Line Number	$^2S_{1/2}$	$^2P_{3/2}$	Wavelength (pm)
D_{2b}	1	F''=1	F'=2	-1.2633
	2		F'=1	-1.2234
	3		F'=0	-1.2051
D_{2a}	4	F''=2	F'=3	0.7197
	5		F'=2	0.7879
	6		F'=1	0.8279

Table 2.2: Transitions from the z^5D state to the z^5F° state.				
$\Delta\lambda$	energy	J''	Energy	J'
(nm)	(cm-1)		(cm-1)	
371.993	0	4	26875	5
373.713	415.9	3	27167	4
374.556	704	2	27395	3
374.826	888.1	1	27560	2
374.59	978.1	0	27666	1
367.991	0	4	27167	4
370.557	415.9	3	27395	3
372.256	704	2	27560	2
373.332	888.1	1	27666	1
368.305	415.9	3	27560	2
370.782	704	2	27666	1

Table 2.3: Populations of the levels in Fe z^5D term	
J value	Population (%)
4	95.86
3	3.74
2	0.34
1	0.05
0	0.01

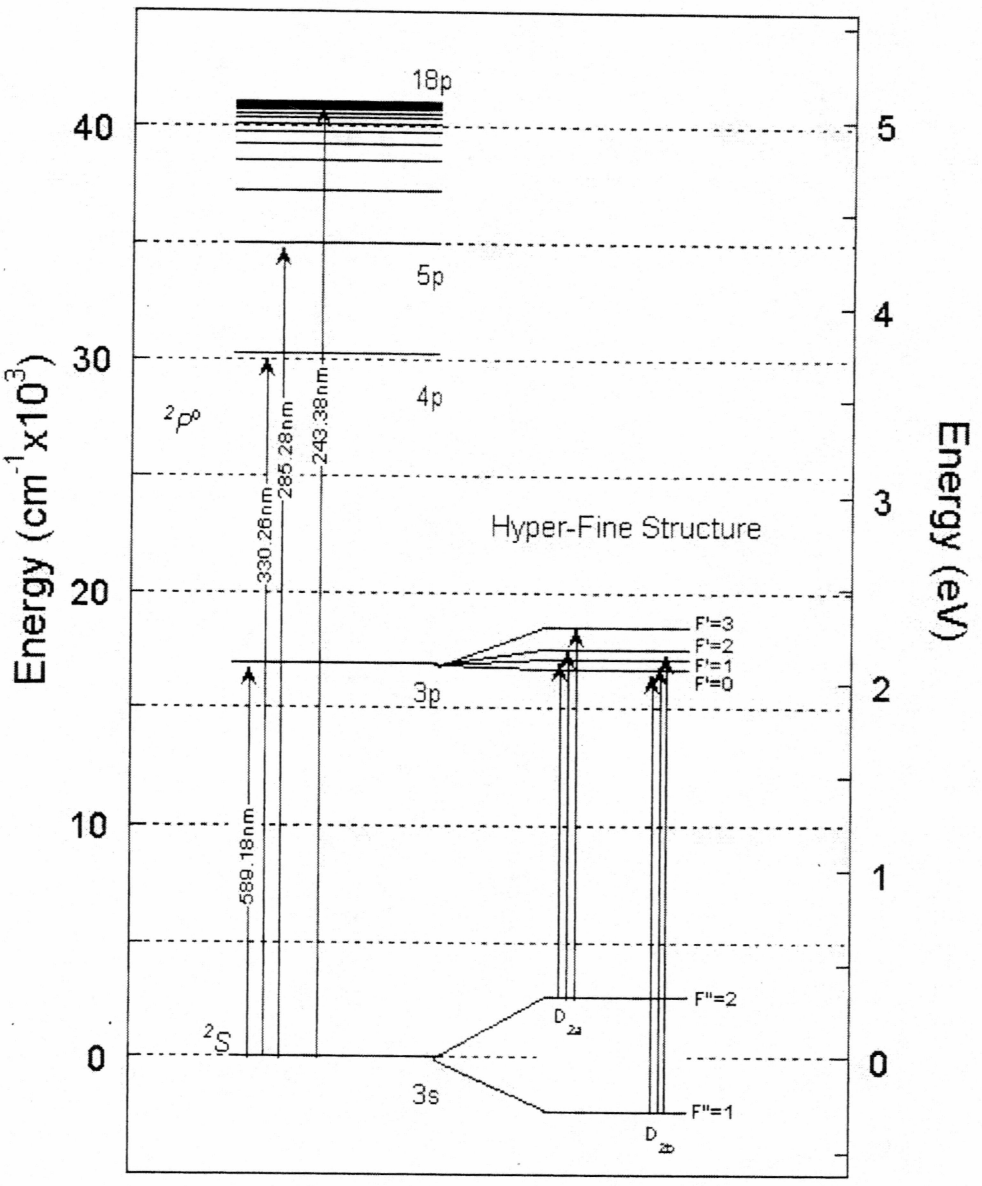

Figure 2.1: The Grotrian Diagram for Na showing the hyperfine structure.

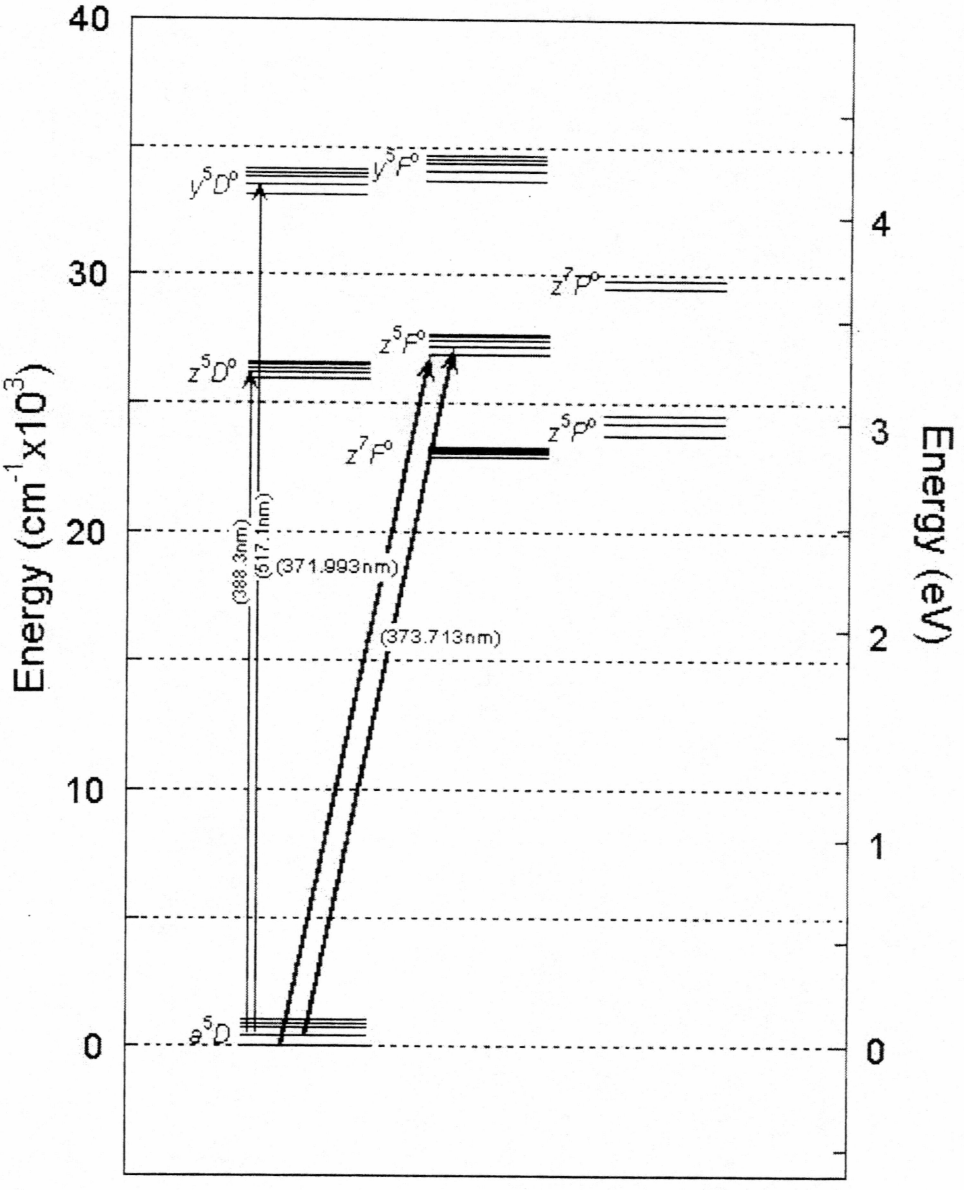

Figure 2.2: The Grotrian diagram for Fe.

Chapter 3: *The Lidar Equation and System performance*

3.1 The Lidar Equation

The lidar equation is used to model the expected lidar signal in terms of the characteristics of the lidar system, the atmosphere and the atom or molecule of interest. From this equation the expected signal from a given height or target in the atmosphere is calculated. The lidar equation takes on a number of forms that can be used for different applications [Measures 1992].

In resonance work, the photons used to measure a particular species are tuned to a specific frequency that matches an energy transition in that target species. These are primarily electronic transitions when examining atomic species. For resonance applications the lidar equation takes the form,

$$N(z) = \left[\eta T^2\right] \cdot \left[\frac{E_L R_L \Delta t}{hc/\lambda}\right] \cdot \left[\rho(z) C_{eff} \Delta z\right] \cdot \left[\frac{A}{4\pi z^2}\right]. \qquad [3.1]$$

Here N (z) is the expected number of photons that are counted by the receiver (i.e. photon counts) from a specific altitude range, z±Δz/2. This

step in range of size $z \pm \Delta z/2$ is termed a range bin because it represents the minimum altitude resolution the measurements are recorded in. We implicitly assume that the altitude resolution Δz is less than the spatial extent of the laser pulse. The equation has been divided into four distinct terms. These terms, from left to right, are; the optical efficiency and atmospheric transmission, the number of photons transmitted, the probability of scattering by the atoms of interest, and the probability of the receiver telescope intercepting the scattered light.

The first term represents the efficiency of the receiver, η, and the two-way transmission of the atmosphere T^2. The efficiency of the receiver includes the transmission of the optics ($\approx$50%) and the quantum efficiency of the photon detector, typically a photomultiplier tube ($\approx$10%). The two way transmission of the atmosphere allows for losses in the signal traveling to and from the mesospheric metal layer. The losses occur predominantly in the troposphere where clouds and aerosols occur also in the troposphere the atmosphere is much denser than in the stratosphere and mesosphere. For clear sky conditions at PFRR the two-way transmission of the atmosphere has a value of $\approx$25%.

The second term is the number of photons transmitted by the laser. The total number of laser pulses is given by the product $R_L \Delta t$, where R_L is the repetition rate of the laser in pulses per second (pps) and Δt is the time

interval over which the measurement is integrated. E_L is the laser pulse energy (J) and (hc/λ) is the energy per photon, where h is Planck's constant (6.63×10^{-34} Js), c is the speed of light (3.00×10^{8} m/s), and λ is the wavelength of the laser light (m).

The third term defines the probability that scattering occurs. The term $\rho(z)$ is the density of scattering atoms (N_1 in chapter 2) (m^{-3}), C_{eff} is the effective scattering cross section and Δz is the range resolution of the measurement. C_{eff} represents the shininess of the scattering atoms and is a function of the laser lineshape as well as the resonance absorption lineshape of the scattering atoms.

Finally the last term represents the fraction of scattered photons that are intercepted by the telescope. Assuming the scattering atoms radiate isotropically then the scattered radiation is uniformly distributed over a sphere of surface area $4\pi z^2$ by the time signal returns to the ground. Thus the telescope of area A intercepts a fraction, $A/(4\pi z^2)$, of the scattered photons.

For Rayleigh scattering the scattering is not isotropic, but has a dipole scattering function. In this case the backscatter cross section used is σ_π^R rather than C_{eff}, where,

$$\sigma_\pi^R = 5.45\left[\frac{550}{\lambda}\right]^4 \cdot 10^{-32}\ m^2/sr. \qquad [3.2]$$

Accordingly the final term of the lidar equation becomes (A/z^2) which is the solid angle in steradians substended by the receiver telescope [Measures, 1992].

From the lidar equation for a resonance system we have,

$$N_S(z) = \frac{K_1 \rho(z) C_{eff}}{4\pi z^2}. \qquad [3.3]$$

Where K_1 is a constant made by combining all the constants not included in this equation from the lidar equation. The Rayleigh photon returns for this same system are,

$$N_R(z_R) = \frac{K_1 \sigma_R^{\pi} \rho_A(z_R)}{z_R^2}. \qquad [3.4]$$

Where K_1 is the same constant and $\rho_A(z_R)$ is the density of the air at altitude z_R. By taking the ratio of the resonance and Rayleigh signals we can get a measurement of the resonance species density, $\rho(z)$, that does not depend on laser power, receiver efficiency, or changing atmospheric conditions,

$$\rho(z) = \left[\frac{N_S(z)}{N_R(z_R)}\right]\left[\frac{z_R^2}{z}\right]\left[\frac{\sigma_R^{\pi}}{C_{eff}}\right]\left[\frac{4\pi}{c}\right]. \qquad [3.5]$$

This is an extremely useful result and shows that the resonance lidar system is self calibrating. As long as the σ_R^{π} and C_{eff} terms are known, no other

constants in the system actually need to be independently calculated to make measurements.

In the ideal case of a dark sky and a noiseless receiver system the above equations would correctly calculate the expected return signal for Rayleigh and resonance lidar work. However, there are stars and other background light in the sky, and the photomultiplier tubes used to measure the signal have noise. To take these additional effects into account the equations used are modified.

$$N_t(z) = N_s(z) + N_b + N_d \qquad [3.6]$$

In this equation $N_t(z)$ represents the total photon counts, $N_s(z)$ represents the total photon counts due to the scattering of laser light, N_b represents the photon counts background sky, and N_d represents the dark counts in the photomultiplier tube (PMT). It is important to note that neither N_b nor N_d are height dependent. These two quantities are constant over the extent of the profile. This property allows the sum ($N_b + N_d$) to be easily determined by taking a measurement of the total counts at a height where there is no laser signal. The term ($N_b + N_d$) is then subtracted from the total (N_t) to get the actual signal counts (N_s).

Photon counting is a statistical process with a Poisson distribution. The actual measurement has a variance equal to the expected value. Thus the signal-to-noise ratio (SNR) may be written as,

$$SNR = \frac{N_s}{\Delta N_s} = \frac{N_s}{\sqrt{N_s + N_b + N_d}}. \qquad [3.7]$$

This statistical uncertainty determines the fundamental trade-off between the resolution and accuracy of the measurement. The measurement can be integrated over time and/or altitude (increasing Δt and/or Δz) to increase the signal levels and obtain the required accuracy at the expense of measurement resolution.

3.2 The Effective Scattering Cross Section

The effective scattering cross section C_{eff}, depends on the laser system used and the atomic transition. C_{eff} results from the overlap between the Gaussian spectral shape of the laser line and the spectral line of the atom. For example, in sodium the D_2 line has a typical full-width-half-maximum (The width of the line, due to lifetime and Doppler broadening, at half the maximum value) of 2 to 4 pm. The absorption cross section (ACS), for this is given by [Verdeyne 1981],

$$ACS = \left[\frac{g_2}{g_1}\right]\left[\frac{\lambda_{D_2} A_{D_2}}{8\pi}\right]. \qquad [3.8]$$

Here λ_{D_2} is the wavelength of the sodium D_2 line, A_{D_2} is the Einstein A coefficient for this transition, and g_1 and g_2 are the degeneracies for the upper and lower states in this transition. This value has units of m^2 and gives the effective area, per atom for scattering a photon of light at the wavelength λ_{D_2}. In real samples, the atoms have thermal velocities and the D_2 line is Doppler broadened. The Doppler broadening allows atoms to interact with photons of light that are not exactly at the λ_{D_2} wavelength. The rms width of this broadening σ_d, depends on the thermal velocity of the atom [Verdeyne, 1981],

$$\sigma_D = \frac{\sqrt{\frac{N_a kT}{M}}}{\lambda}. \qquad [3.9]$$

Where N_a is Avagadro's number (6.02×10^{23} mol^{-1}), k is Boltzmann's constant (1.38×10^{-13} J/K), M is the molecular or atomic mass (kg), λ is the wavelength of the transition (m), and T is the temperature (K).

A tunable laser can probe the wavelength dependence of C_{eff}. When the laser wavelength is identical to the center wavelength of the transition ($\lambda_L = \lambda_{D_2}$), C_{eff} is a maximum. This maximum value is given by [Verdeyne 1981],

$$C_{eff\,max} = \frac{ACS}{2\pi\sigma_E} \text{ where } \sigma_E = \sqrt{\sigma_D^2 + \sigma_L^2}. \qquad [3.10]$$

Where σ_L^2 is the rms width of the laser line. C_{eff} then, is the effective scattering cross section per atom based on the laser and transition characteristics.

3.3 Data Collection

From the lidar equation we see that a raw data profile can be acquired from a number ($R_L \Delta t$) of laser shots. This is an individual profile with a basic resolution defined by Δt and Δz. The raw profiles can subsequently be integrated in time, by summing a series of profiles, or in space, by summing a series of range bins, to yield a given statistical significance for numerical analysis of the data. Therefore we collect the data at the highest resolution (smallest Δt and Δz) that allows us to assess the data quality in real time. Typically resonance data is collected at a resolution of $\Delta t \approx 500$ to 1000 integrated laser shots and $\Delta z \approx 75$ m to yield an individual profile. An example of the real-time data acquisition display is shown in Figure 3.1. Profiles are further collected into sets of profiles. For example shown in Figure 3.1 are profiles 1 through 8 of set 30 for the night of 1-2 December 2000. Listed is the profile number, the time, photon counts from various altitudes, the total signal is calculated for the metal layer, and the 'per shot'

is the photon counts received from the metal layer per shot of the laser. In the bottom of Figure 3.1 is a plot of each profile.

While profiles make up the highest resolution that the lidar data is collected, sets are arbitrary groups of these profiles. There are several purposes for grouping the profiles into sets that make the file size manageable and divide the data into logical groups. Grouping data collected at a particular wavelength setting simplifies the handling of the data by collecting similar profiles into sets; each saved to one file. For example, one set may contain profiles taken at a wavelength λ_1 while then next set may contain profiles taken at a different wavelength λ_2. This distinction, imposed during data collection, simplifies the archiving and processing of data.

Profiles represent the smallest resolution the data is stored as and is a collection of photon returns or shots taken. Sets are then arbitrary or logical groupings of these profiles used to simplify data storage and processing and correspond to individual data files. These two structures make up a data-set for a given night.

Set 30 02/12/00 DC01LP Shots 800 Lat 65.00 Long 147.00

Profile	Time	Ray	60-80	80-100	100-120	Tot. Sig.	Per Shot
1	00:18:53	15	2398	5711	2473	3313	4.1
2	00:19:36	13	2462	5654	2363	3192	3.9
3	00:20:17	13	2222	5915	2330	3693	4.6
4	00:20:58	23	2383	5875	2390	3492	4.3
5	00:21:39	7	2546	6289	2587	3723	4.6
6	00:22:22	9	2635	6318	2752	3683	4.6
7	00:23:03	7	2479	6437	2719	3958	4.9
8	00:23:47	19	2351	6263	2327	3912	4.8

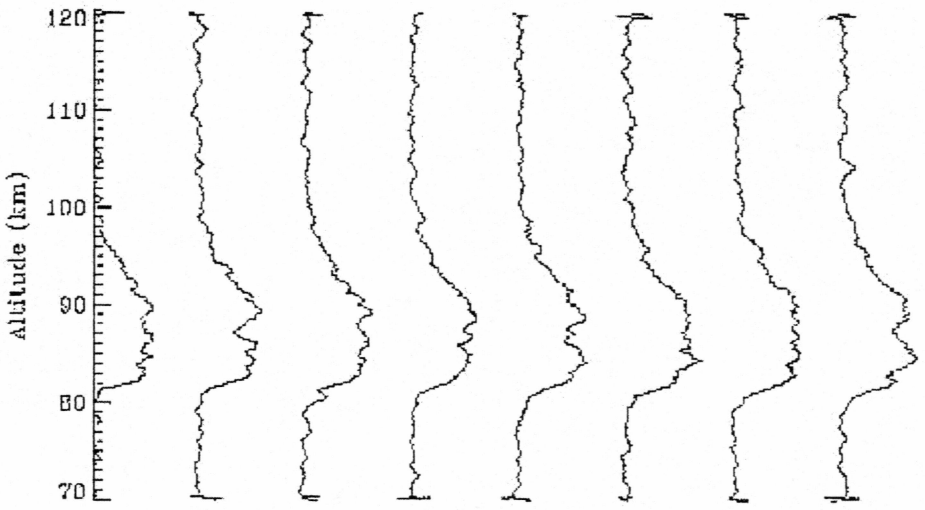

Figure 3.1: Acquisition display on the night of 1-2 December 2000 for profiles 1 to 8 of set 30. The Na layer is clearly visible between 80 and 100 km.

Chapter 4: *Na Calibration and Measurements*

4.1 Introduction

In this chapter we analyze the performance of the lidar measurements of the mesospheric Na layer. We compare the performance of the flashlamp-pumped dye laser system (the LFDL-1 laser) and the excimer-pumped dye laser system (the LPX210i and Scanmate 2 dye laser). We also study the tuning stability of the Lambda Physik laser system by making Na lidar measurements at 1 pm resolution.

4.2 Comparison of laser systems

On the night of 6-7 November 2000, lidar measurements of the Na layer were made with both the flashlamp-pumped (LFDL-1) and excimer-pumped (Scanmate 2) dye lasers. While the laser transmitter was changed during the night, the receiver system remained the same in both cases. The photon count profiles are plotted in Figure 4.1. The photon count profiles represent the signal obtained over 2000 laser shots. For the Scanmate 2

system the data represents the data taken for all of set 12, 4 profiles of 500 laser shots each. For the LFDL-1 the data represents all of set 19, 8 profiles of 1000 shots each. The LFDL-1 data was divided by 4 to have a direct, 2000 shot comparison between the two systems. The photon count results used in the comparison are summarized in Table 4.1.

From the Rayleigh signal we see that the Scanmate 2 laser has (1430/273) = 5.2 times more energy per pulse than the LFDL-1 laser. The Rayleigh signal has a relatively weak (λ^{-4}) dependence on wavelength and laser linewidth so the difference represents a difference in energy per pulse. For the resonance counts we see that the Scanmate 2 laser yields resonance signals (9258/774) = 12 times larger than the LFDL-1 laser. While 5.2 of this is due to the differences in laser energy (12.0/5.2) = 2.3 of this is due to the differences in C_{eff}. The Scanmate 2 laser has a narrower lineshape and more stable wavelength (i.e. ν_L remains constant) than the LFDL-1 laser. Furthermore the LFDL-1 operates at 7.5 Hz while the Scanmate 2 laser operated at 20 Hz. In terms of the lidar equation the Scanmate 2 increased E_L by a factor of 5.2, C_{eff} by a factor of 2.3, and R_L by a factor of 2.7 relative to the LFDL-1. For a given resolution (Δt, Δz) the Scanmate 2 will yield 32 times more signal than the LFDL-1. In general the Scanmate 2 can operate at 50 Hz and this increases the improvement to 81 times that of the LFDL-1.

4.3 Experimental Determination of C_{eff}

From chapter 3 we have determined C_{eff} as a function of absorption linewidth and laser linewidth. For analysis of Na the absorption feature appears as a doublet with the feature modeled as two Gaussian curves [Bills et. al., 1991]. This fine structure doublet is an approximation to the hyperfine structure which involves six transitions [Fricke and von Zahn, 1988]. Thus the effective scattering cross section can be modeled as,

$$C_{eff} = \sigma_a \cdot \exp -((\nu_L - \nu_a)^2/(2\sigma_e^2)) + \sigma_b \cdot \exp -((\nu_L - \nu_b)^2/(2\sigma_e^2)) \qquad [4.1]$$

where

$$\sigma_a = (20/32)\cdot((A_{21}\lambda^2)/(16\pi^2\sigma_e)) \qquad [4.2]$$

and

$$\sigma_b = (12/32)\cdot((A_{21}\lambda^2)/(16\pi^2\sigma_e)). \qquad [4.3]$$

For our analysis we make lidar measurements at a series of wavelength settings. If the Na density and the system parameters remain constant then the measured lidar signal is proportional to the effective scattering cross section. From the lidar equation

$$N_s(\nu_1)/N_s(\nu_2) = C_{eff}(\nu_1)/C_{eff}(\nu_1) \qquad [4.4]$$

The changes made for measuring the hyperfine linewidth are less than 20 pm at a wavelength of 589 nm (i.e. one part in 29,000) so it can be assumed that there is no significant change in any of the other lidar system parameters.

We carried out this analysis three times on the night of 3-4 November 1999. The experimental details are listed in Table 4.2. In each case the total number of photon counts is summed over the altitude of the Na layer, at 70 to 110 km, as the signal at that wavelength. The signals $N_s(\nu_1)$ are then normalized to $C_{eff}(\nu_1)$ using the equation

$$C_{eff}(\nu_i) = kN_s(\nu_i) \qquad [4.5]$$

where

$$k = \frac{\sum_{i=1}^{n} C_{eff}(\nu_i) \cdot N_s(\nu_i)}{\sum_{i=1}^{n} N_s(\nu_i) \cdot N_s(\nu_i)} \qquad [4.6]$$

The centroid $\bar{\nu}$ of $N_s(\nu_i)$ is used as the centroid of the expected $C_{eff}(\nu_i)$. To match the peak of the spectra with the peak of the model, all the points of the measured shape that were within 25% of the maximum value were used to locate the peak. Then once the peaks of the two spectra were aligned, and scaled, any points within 75% of the maximum value were used to compare the two functions. Using values less than 75% of the maximum value cause the fit to be skewed, by fitting to regions of spectra that are dominated by noise. The regions used for matching the spectra are shown in

Figure 4.2. Three tuning curves were taken throughout the night of 3-4 November 1999, and each were fitted to the model in the manner described above and are shown in Figures 4.3, 4.4 and 4.5.

For the night of 3-4 November 1999, we found from the three different tuning measurements that the measured C_{eff} was consistent with a laser linewidth between 3.25 and 4.0 pm and a temperature between 150 and 250 K. This value of the measured linewidth is slightly narrower than the manufacturer quoted linewidth of 5.2pm. Note that the width of the laser line obscures the dip in the sodium D_2 spectrum. True hyperfine temperature measurements require a laser linewidth of 0.1 pm.

4.4 Validation of the Lidar Equation

Given that we have calculated C_{eff} for the lidar system, we can now determine the Na density from the photon count data following equation 3.5. Furthermore, once the densities are calculated we can determine the value of the optical efficiency and atmospheric transmission term in the lidar equation. We consider set 71 from the night of 3-4 November 1999. The values are listed in Table 4.3. We find that for the resonance signal

$$(\eta T^2)_{res} \approx 5.0 \times 10^{-3}$$

while for the Rayleigh signal

$$(\eta T^2)_{ray} \approx 4.4 \times 10^{-3}.$$

These two values are in good agreement with each other. Taking the resonance estimate and assuming the atmospheric transmission is 50% (25% for two way transmission) we find that

$$\eta \approx 0.02.$$

For the receiver the quantum efficiency of the photomultiplier tube is approximately 0.2, the transmission of the 3 Å bandpass filter is also approximately 0.25 which suggests that the receiver efficiency should be 0.05. Small alignment issues in the alignment of the receiver, and transmission losses (≈20%) yield an expected efficiency of 0.04. The mismatch by a factor of two is well within the expected values since the transmission of the bandpass filter and the efficiency of the photomultiplier tube are expected to decrease with age, and both were purchased in 1994.

Table 4.1: Raw photon counts from 3-4 November 1999				
	Rayleigh	Resonance	Background	Total Shots
Bin count	13	267	67	
Lambda-Physik	1576	12075	707	2000
Candela	1152	4316	306	8000
After background subtraction				
Lambda-Physik	1430	9258		2000
Candela	1093	3096		8000
Candella*0.25	273	774		2000

Table 4.2: C_{eff} values for the Na Tuning Curves for 3-4 November 1999.			
Starting set	Ending set	SCA (m^{-2})	Laser Linewidth
1	6	4.08E-16	3.3
9	16	3.52E-16	4.0
61	71	3.52E-16	4.0

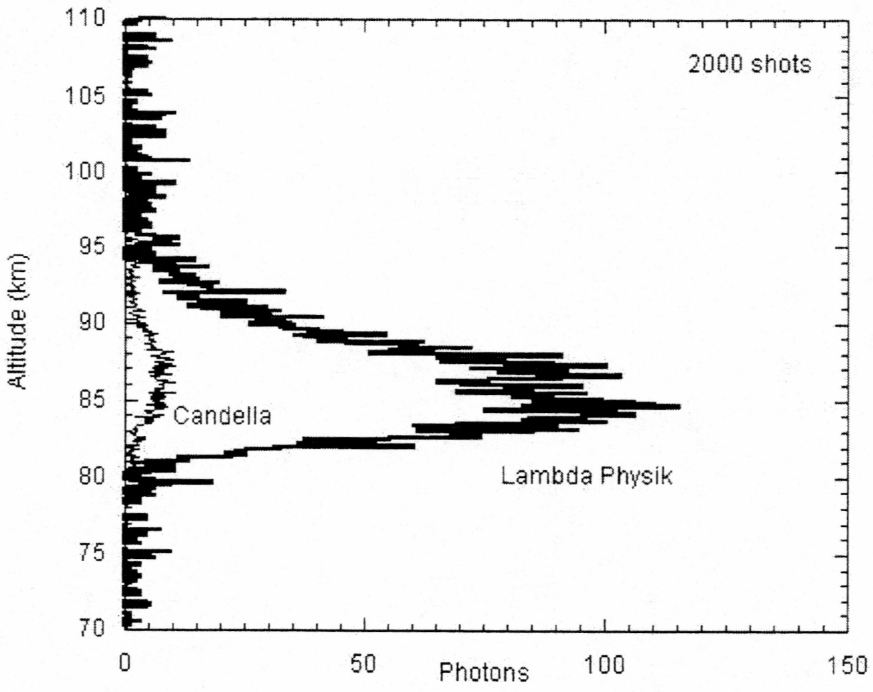

Figure 4.1 Photon count comparison between the Lambda Physik lidar and the Candela lidar with an equivalent number of shots (2000) on the night of 6-7 November 2000. Set 12 was used for Lambda Physik, and set 19 was used for Candela.

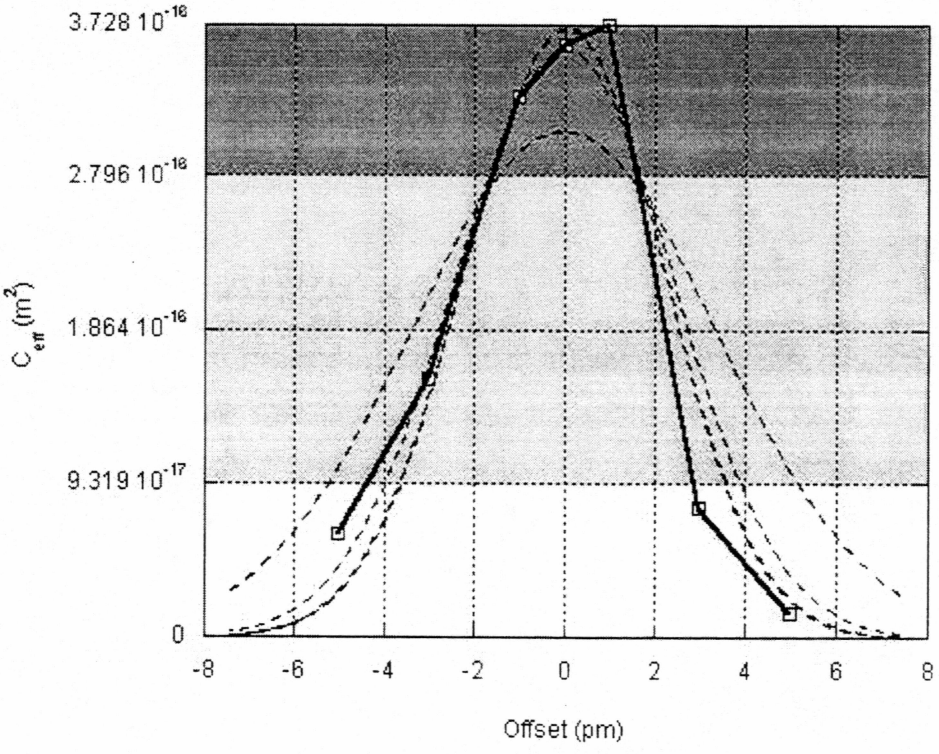

Figure 4.2: Regions used for fitting. Points that fall within 25%, (dark gray area), of the maximum value are used to match the peak of the spectral line with the peak of the model. Points within 75%, (light gray area), of the maximum value are used to calculate the difference between the spectral line and the model. Points greater than 75% away from the maximum are discarded from fitting (white area).

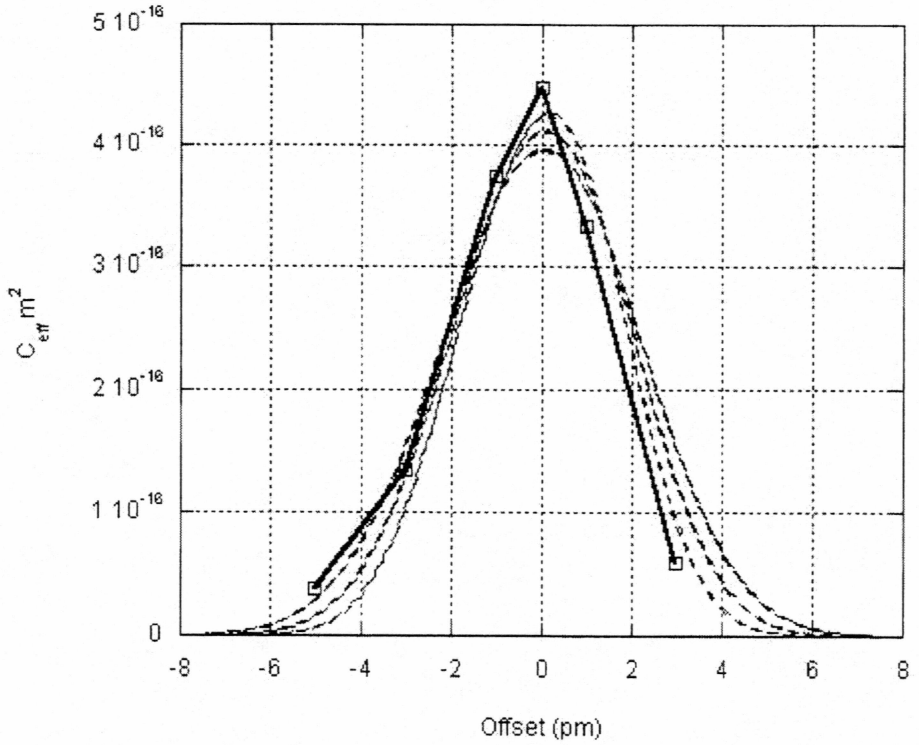

Figure 4.3: The first Na tuning measurement from the night of 3-4 November 1999. This is made from sets 1 through 6.

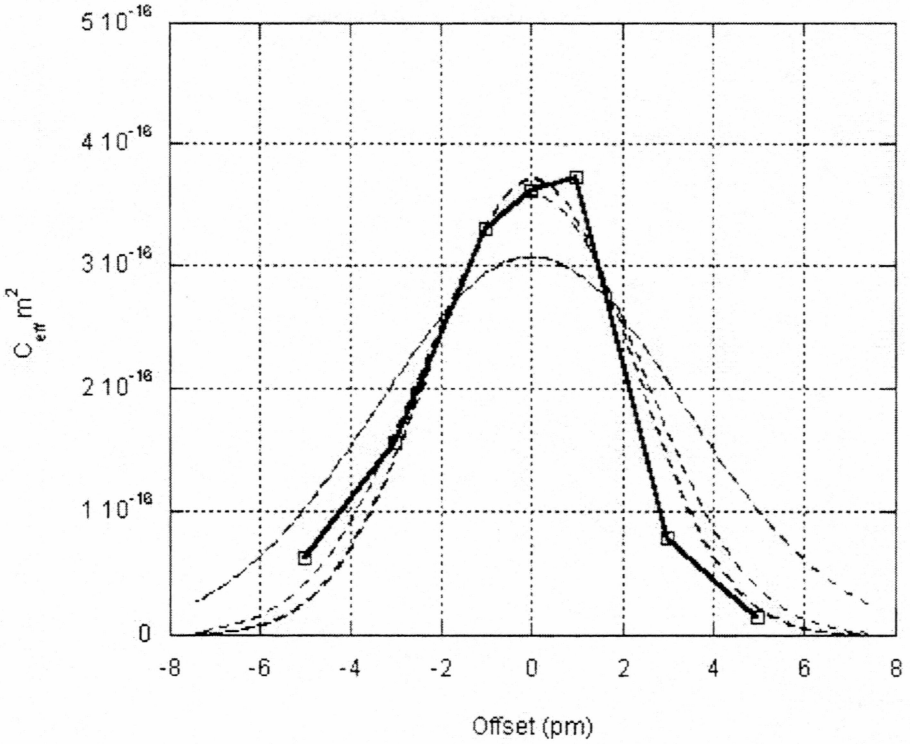

Figure 4.4: The second Na tuning measurement from the night of 3-4 November 1999. This is made from sets 9 through 16.

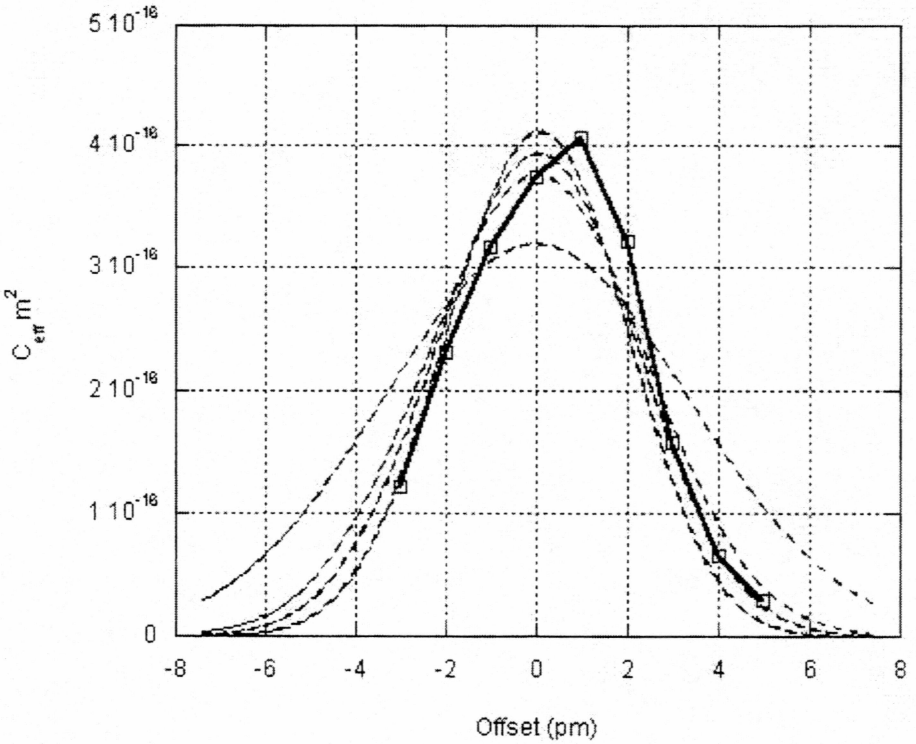

Figure 4.5: The third Na tuning measurement from the night of 3-4 November 1999. This is made from sets 61 through 71.

Chapter 5: *Fe Calibration and Measurements*

5.1 Introduction

In this chapter we analyze the performance of the lidar measurements of the mesospheric Fe layer. Following our analysis of the mesospheric Na measurements, we first determine the effective scattering cross section, C_{eff}. We then validate the lidar equation. Finally, we make Fe lidar measurements at 372 and 374 nm to assess the ability to make Fe Boltzmann temperature measurements.

5.2 Experimental Determination of C_{eff}

From chapter 2 Fe has two spectral lines at 372 and 374 nm. The features at each wavelength have Gaussian lineshapes. In this section we show how the scattering cross section is determined. For Fe the populations in the lower state are determined by Boltzmann population statistics. At a temperature of 200 K 3.7% of the iron population is in the a^5D_3 state, and 95.9% is in the a^5D_4 state. Thus the lidar equation contains an extra term for

the population of the state being excited. The lidar signal for the 374 nm line will be approximately 26 times less than that for the 372 nm line. The measured effective scattering cross section is plotted in Figure 5.1. This measurement was made on the night of 13-14 December 2000. The experimental results are presented in Table 5.1. From Figure 5.1 we see that the Fe line is narrower than the Na line (Figures 4.3, 4.4, 4.5). This is in part due to the fact that the Na line is a doublet represented by the superposition of two Gaussian functions separated by about 2 pm. Furthermore, the use of a wavelength scale rather than frequency scale makes the Fe line at 372 nm appear narrower than the Na line at 589 nm. A change in frequency of 1 GHz at 372 nm is equivalent to a wavelength change of 0.5 pm, while at 589 nm it is equivalent to a change of 1.2 pm. The curve fit indicates that the laser linewidth is 1.25 pm (≈2.5 GHz) and the Fe temperature in the range of 140 to 290 K. The effective scattering cross section is 3.6×10^{-17} m^2.

5.3 Validation of the Lidar Equation

Having determined the effective scattering cross section we can now determine the Fe density from the photon count data following Equation 3.1. Once the Fe density is calculated the value of the optical efficiency and the

atmospheric transmission term in the lidar equation. We consider set 8 from the night of 13-14 December 2000. The values are listed in Table 5.2 the altitude ranges were 34.5 to 35.5 km for Rayleigh, 83 to 84 km for resonance and 125 to 126 km for background photon counts. For comparison we also consider the performance of the CRL telescope for the Rayleigh measurements at 532 nm. For resonance and Rayleigh signal at 372 nm we find

$$(\eta T^2)_{res} = 1.6x10^{-3}$$

and

$$(\eta T^2)_{ray} = 1.6x10^{-3}.$$

For the Rayleigh signal at 532nm we find

$$(\eta T^2)_{ray} = 8.7x10^{-3}.$$

The lidar receiver was designed for work at 532 nm and thus we expect a decrease in the optical efficiency and transmission of the atmosphere. If atmospheric scattering, and hence attenuation, varies with wavelength as a power law dependence with a power of 2 to 4 we expect a reduction in atmospheric attenuation by a factor of 2.1 to 4.2. We expect the receiver efficiency to be further reduced due to lower receiver telescope mirror reflection and transmission through the receiver glass optical elements in the UV.

5.4 Mesospheric Fe Densities

In calculating the Fe density, Equation 3.5 was used. The background counts were taken at 125 km, and the Rayleigh altitude counts were taken at 35 km. On the night of 15-16 December 2000, temperature data measurements were collected. They consisted of three 372 nm tuning sets, and alternating 372 and 374 nm data-sets. The 372 nm resonance line measurements yielded approximately one count per shot signal returns and were collected in 48,000 shot sets. The 374 nm resonance line yielded approximately 0.2 counts per shot and was taken in 144,000 shot sets. A total of 12 data-sets were taken making five pairs of temperature measurements (five 372nm and 374nm resonance line sets) with two 372nm resonance line sets taken at the close of the evening. The last two sets were taken consecutively to determine if the layer was evolving over the time scale of our data-sets. The photon count statistics for the night are given in Figure 5.2 and show that there were no large-scale changes in the layer over the time scale of the observations. This indicates that the Fe densities were relatively constant, or that the Fe layer was stable, over the observation period. The only large fluctuation is due to the different number of shots per profile for tuning measurements and the different temperature

measurements. For sets with equal numbers of shots the statistics are constant.

Data taken on the night of 13-14 December 2000 provide an example of what a stable Fe layer is. Figure 5.3 shows the Fe density profiles calculated from the photon count data of 13-14 December 2000. These measurements are within the expected density ranges for Fe in this season [Kane et. al., 1992; Alpers et. al., 1990]. The peak density was 1.1×10^5 atoms/cm^3, and the atomic Fe layer occurred between 75 and 95 km in height. This is what the layer on the night of 15-16 December 2000 would have looked like if the data collected over the evening were all at a single wavelength, as indicated by the photon counts. The same visualization is not apparent for 15-16 December 2000 because the wavelength was changed regularly throughout the night as different species were measured.

5.5 Fe Temperature Calculations

Once the densities of Fe have been calculated for the 374 nm and the 372 nm resonance lines it is a direct calculation of temperature through the Equation 2.5,

$$T = \frac{(\Delta E)}{k \ln\left(N_{372} g_{374} / N_{374} g_{372} \right)}. \qquad [5.1]$$

Since it was shown earlier that the populations in the states other than the two we are measuring are negligible, it can be assumed that all of the atoms are in either the N_{372} or N_{374} populations.

To get a temperature for a given time period, three data-sets were used for each temperature measured. Temperature sets consisted of two measurements of the layer at one wavelength and a third at the other wavelength. This gave us an average for the layer during the time the middle wavelength was taken. So each temperature is the product of three data-sets. The calculated temperatures are presented in Table 5.3.

The first important observation is that the temperature appears to vary greatly throughout the night. Over the course of the measurements the temperature changes by 30%. This is far too large of a variation, and is not expected. Also of note is that most of the temperatures appear to be lower than the expected temperatures for this time of the year [Bilitza, 2001].

5.6 Error in Temperatures

The measured linewidth of the laser operating at atomic Fe wavelengths was 1.25 pm, or 3 GHz. The laser linewidth measured for Na was ≈4 pm, or 3 GHz. This shows that the apparent linewidth change is due to the differences between wavelength and frequency. The linewidth in gigahertz does not actually change.

Also of note is that comparing the linewidth over such a large distance in wavelength is not a good practice. The two systems, Na and Fe, while using the same physical laser, use completely different dyes and solvents to achieve lasing. Also the physical selection of the light in the laser is performed by a grating, which will have different light separating properties in the blue portion of the spectrum as compared to the red or yellow portion of the spectrum. As the color of the light shifts toward the blue, the grating provides less wavelength resolution. This is apparent in the mechanical portion of the laser system. Mechanically the system steps through in a constant step of 1 pm. This causes our step-size in gigahertz to change as we move across the spectrum. For example, at 589 nm, a 1 pm step-size is equal to a 0.86 GHz step-size, while at 374 nm; the same 1 pm step-size is now equal to a 2.16 GHz step-size. The difference between wavelength and frequency for a given color of light is shown in Figure 5.4.

Since the step-size is getting larger in gigahertz, errors in the correct measurement of the location of the Fe peak become very important. If we assume that we are correctly online at the Fe 372 nm resonance line, and that all the error in the measurement is due to the errors in the alignment of the laser tuning with the Fe 374 resonance line, the error can be calculated.

From Boltzmann's equation, the actual temperature, T, and the measured temperature, $\tilde{T}$, are,

$$T = \frac{(\Delta E)}{k \ln\left(N_{372} g_{374} / N_{374} g_{372} \right)} \qquad [5.2]$$

$$\tilde{T} = \frac{(\Delta E)}{k \ln\left(N_{372} g_{374} / \tilde{N}_{374}\, g_{372} \right)}. \qquad [5.3]$$

Here the change in energy is ΔE, k is Boltzmann's constant, N_{372} is the population and g_{372} is the degeneracy of the 0.0 cm^{-1} energy ground state, and N_{374} is the population and g_{374} is the degeneracy in the first thermally excited 415.9 cm^{-1} energy ground state. $\tilde{N}$ is the incorrect measurement of the population of the excited state due to incorrect frequency selection.

$$\tilde{N}_{374} = N_{374} e^{-\frac{1}{2}\frac{\Delta\nu^2}{\sigma^2}} \qquad [5.4]$$

Where $\Delta\nu$ is the offset of the laser from line center (cm^{-1}), σ is the combined width of the two Gaussians, $\sigma^2 = \sigma_L^2 + \sigma_D^2$. σ_L is the Gaussian width of the laser line, and σ_D is the Doppler width of the spectral line. If the laser were a perfect monochromatic source, then $\sigma_L \to 0$, and $\sigma^2 \to \sigma_D^2$. We can write the error in the form of,

$$\frac{\tilde{T}}{T} = \frac{1}{1 + \left(\frac{\Delta\nu^2}{2\sigma^2}\right)\frac{1}{A}} \qquad [5.5]$$

where

$$A = \ln\left(\frac{N_{372}}{N_{374}}\right). \qquad [5.6]$$

Combining this with Boltzmann's equation, we get:

$$\frac{\tilde{T}}{T} = \frac{1}{1 + f(\Delta\nu)} \qquad [5.7]$$

where

$$f(\Delta\nu) = \frac{M\lambda^2\Delta\nu^2}{N_a\Delta E}. \qquad [5.8]$$

From this it is apparent that $\tilde{T}$ can only approach T, and in fact the measured temperature will always be less than the actual temperature ($\tilde{T} \le T$). Table 5.4 gives the error in T for a given value of $\Delta\nu$ and this dependence is

plotted in Figure 5.5. Just a small error in the location of the maximum C_{eff} (≈0.25pm) quickly leads to significant changes in the measured temperature (≈20%).

5.7 Gradient in Temperature Measurements

The errors in the laser tuning will bias both the topside and the bottomside temperatures by the same fraction. Thus, while the absolute temperature measurements are biased, the ratio of the topside and bottomside measurements made at the same time will not be biased. The ratio of the topside to the bottomside temperatures are presented in Table 5.5. We see that the ratio shows a systematic behavior throughout the night, where the top side of the layer is always colder than the bottomside. The ratio value of 0.9 is consistent with the MSIS-E results for this time of the previous year [Bilitza, 2001]. Thus we have confirmed that the wintertime mesopause is above the Fe layer at PFRR similar to mid-latitude lidar observations [Senft et. al., 1994].

5.8 Seasonal Variation in Measurements

During the winter months there is more atomic Fe present in the mesosphere. The seasonal variation of Fe has been reported to be quite high [Kane et. al., 1992; Kane and Gardner, 1993] and was readily apparent in measurements made from December 2000 to March 2001 with a maximum in winter and a minimum in summer. Table 5.6 presents the photon counts per shot for some data-sets collected over this time period, and it is clear that the abundance of Fe is decreasing. Measurements of temperature are not possible with the low abundances seen for Fe in March. For a measurement of temperature Fe photon counts need to be at least 1 count per shot for the 372 nm resonance line of Fe. This would give returns of 0.1 count per shot for the 374 nm resonance line, which would be marginal data requiring long integration times to achieve a signal that is statistically significant.

Table 5.1: C_{eff} values for the Fe Tuning Curves for December 15 2000.			
Starting set	Ending set	SCA (m^{-2})	Laser Linewidth
1	5	$3.55x10^{-17}$	1.25

Table 5.2: Raw photon counts from 13-14 December 2000				
	Rayleigh	Resonance	Background	Total Shots
Bin count	13	14	14	
Lambda-Physik	30,009	10,822	826	8,000
Bin count	13		67	
Rayleigh	7,200,000		3,810	320,000
After background subtraction				
Lambda-Physik	2,9242	9,996		8,000
Rayleigh	7,199,204			8,000

Table 5.3: Mesospheric temperatures derived from Fe densities.	
Measurement	Temperature (K)
1	169
2	183
3	198
4	207
5	209
6	205
7	204
8	228
9	256

Table 5.4: Error in Temperatures due to miss-alignment of lidar with peak C_{eff}			
	Temperature		percent
offset (pm)	Measured	ΔT	error
0.0	200.0	0.0	0.0%
0.1	193.0	7.0	3.5%
0.2	174.7	25.3	12.6%
0.3	150.9	49.1	24.5%
0.4	126.7	73.3	36.6%
0.5	105.1	94.9	47.5%
0.6	86.9	113.1	56.5%
0.7	72.2	127.8	63.9%
0.8	60.4	139.6	69.8%
0.9	50.9	149.1	74.5%
1.0	43.3	156.7	78.3%

Table 5.5: Temperature gradient across the Fe layer			
set	70-85 km	85-100 km	Ratio
1	178	156	0.87
2	190	173	0.91
3	209	182	0.87
4	223	187	0.84
5	219	196	0.89
6	219	185	0.84
7	219	178	0.81
8	237	210	0.88
9	269	231	0.86
Average	218	188	0.86
Stdev	26	22	0.03
MSIS-E	229	201	0.88

Table 5.6: Seasonal variation in measurements of Fe densities	
Date	photon counts per shot
15-Dec	≈2.0-3.0
19-Feb	≈0.5
23-Feb	≈0.25
17-Mar	≈0.15

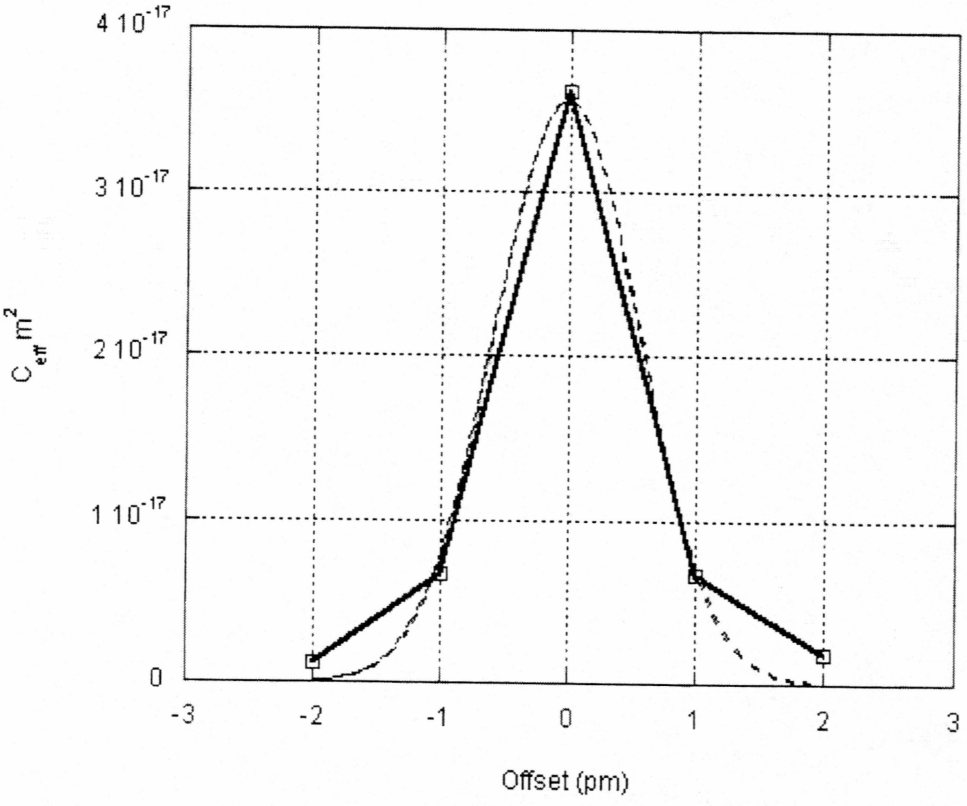

Figure 5.1: Fe tuning measurement from the night of 15-16 December 2000. This is made from sets 1 through 5.

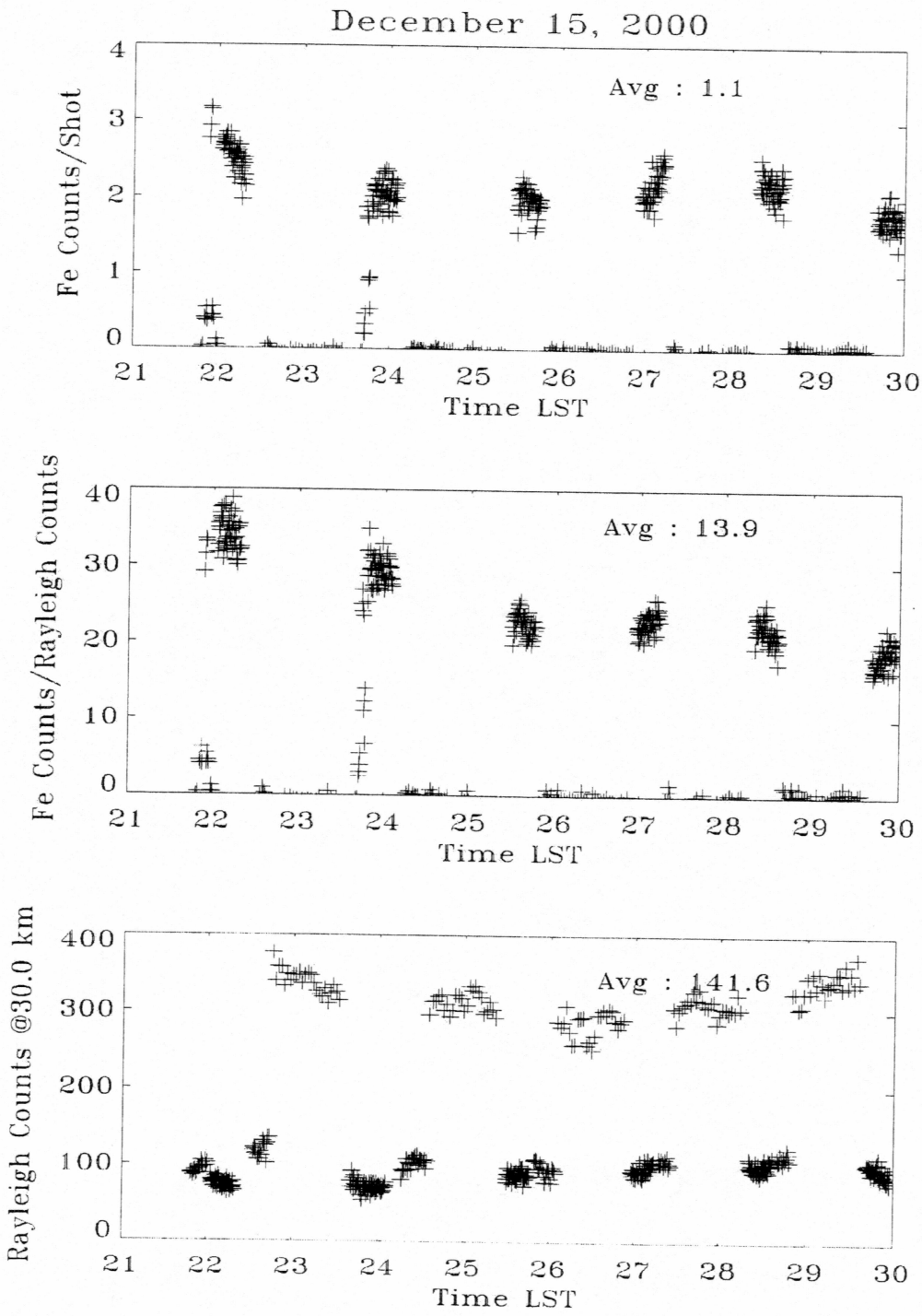

Figure 5.2: Fe photon count statistics from the night of 15-16 December 2000.

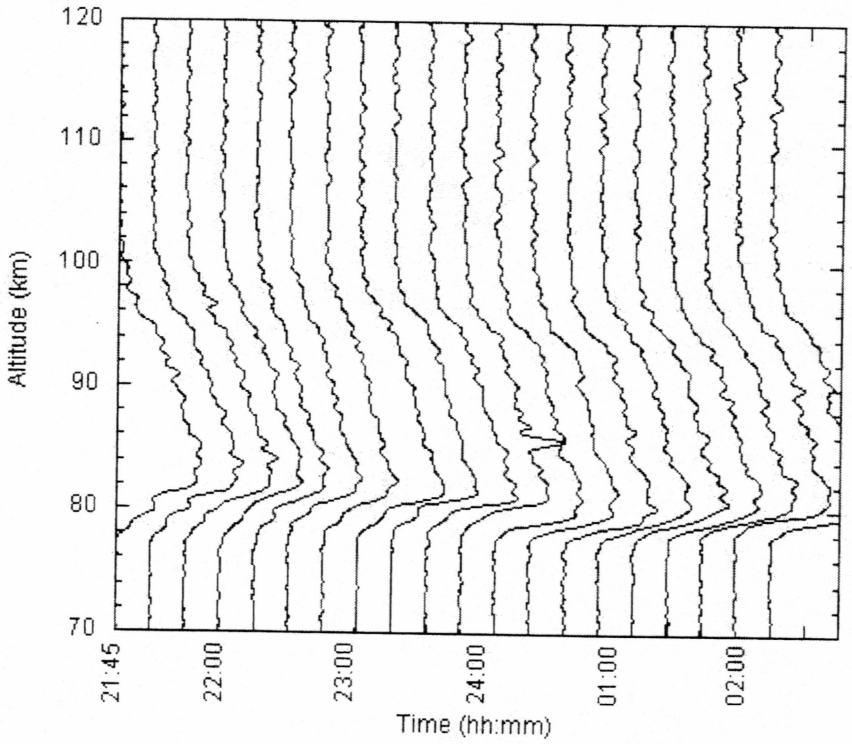

Figure 5.3: The Fe density for the night of 13-14 December 2000.

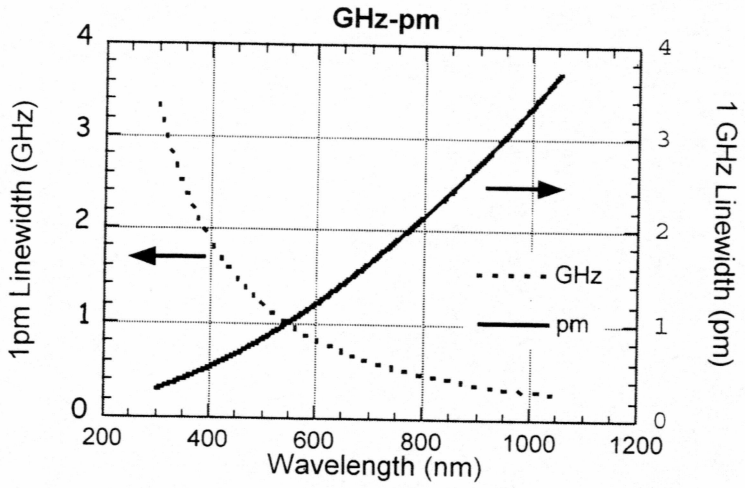

Figure 5.4: Change in linewidth measurement of picometers and gigahertz versus wavelength.

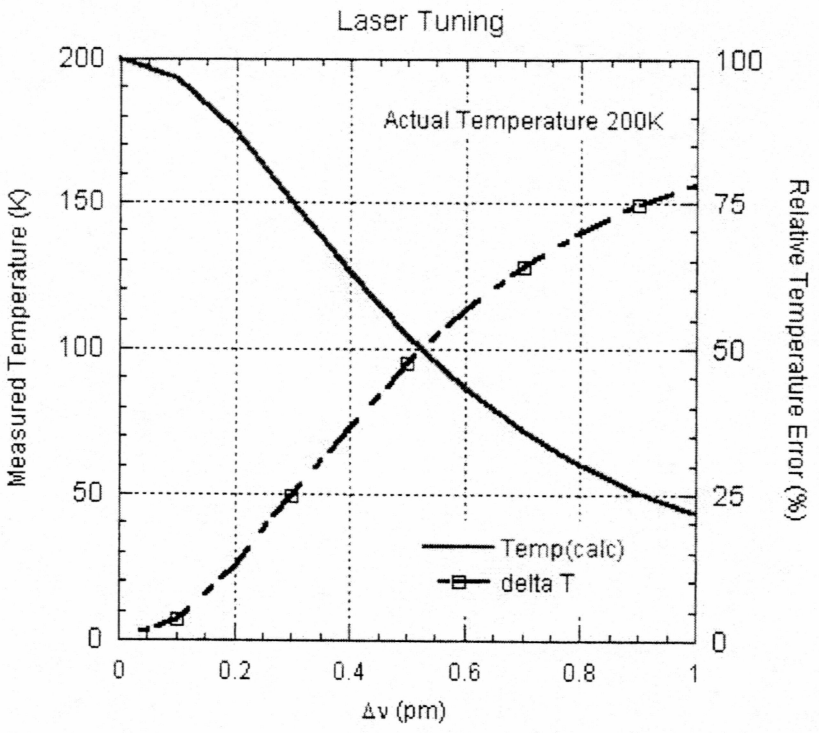

Figure 5.5: The variation in temperature due to a misalignment with the Fe 374 resonance line.

Chapter 6: *Conclusions and Further Work*

6.1 Conclusions and Further Work

The new lidar at PFRR works well at Na wavelengths. In comparison to the current Candela based system, the Lambda Physik lidar provided a factor of eleven increase in signal levels on a per shot basis. A factor of 5.2 was due to the increased output power, and a factor of 2.7 was due to improvements in the quality of the laser line shape. The increased signal information allows easy comparison between the data taken with the Lambda Physik system and the Candela system. The new system allows for higher resolution measurements to be taken as needed.

The Lambda Physik lidar is also able to take measurements of the mesospheric Fe layer. The high output power and improved line shape quality of the Lambda Physik yields Fe signal levels that are comparable to the returns from the Candela based system operating on Na. This similarity across metals will allow the simultaneous measurement of Fe and Na at the site, for possible future work in investigating sporadic mesospheric metal layers.

Temperature measurements were also made and the signal levels of the system when it was properly aligned to the Fe resonance line are large enough to get reasonable measurements of temperature. However these measurements are very sensitive to the alignment of the laser frequency with the resonance line. Small differences in alignment lead to large temperature errors. To make accurate mesospheric temperature measurements the grating scanning system needs to be adjusted such that 0.3 pm steps can be taken. This reduction in step-size would allow for more points on the iron line spectra to be measured. If more points on the spectrum were known, then even if the system could not be tuned to the peak of the effective scattering cross section function, the location of the actual laser frequency in relation to the peak would be known. With this knowledge, the temperature measured could be adjusted to give a more accurate indication of the actual temperature. An adjustment like this is possible, and would allow the measurement of actual temperatures in addition to the current measurements of temperature gradients.

Bibliography

Aberty, R. A., Physical Chemistry, John Wiley and Sons, New York, 1983

Alpers, M., Höffner, J., von Zahn, U., Iron Atom Densities in the Polar Mesosphere from Lidar Observations, Geophysical Research Letters, 17, 12, 2345-2348, 1990

Andrews, D. G., Holton, J. R., Leovy, C. B., Middle Atmosphere Dynamics, Academic Press, Orlando, FL, 1987

Atkins, P. W., Quanta: A Handbook of Concepts, Oxford University Press, New York, 1991

Atkins, P. W., Physical Chemistry, W. H. Freeman and Co., New York, 1994

Bernath, P. F., Spectra of Atoms and Molecules, Oxford University Press, New York, 1995

Bilitza, D., MSIS-E 1990 Atmospheric Model [Online], available http://nssdc.gsfc.gov/space/model/models/msis.html, accessed May 19, 2001

Bills, R. E., Gardner, C. S., Lidar Observations of Mesospheric Fe and Sporadic Fe Layers at Urbana, Illinois, Geophysical Research Letters, 17, 2, 143-146, 1990

Bills, R. E., Gardner, C. S., Narrowband lidar technique for sodium temperature and Doppler wind observations of the upper atmosphere, Optical Engineering, 30, 1, 13-21, 1991

Brasseur, G., Solomon, S., "Aeronomy of the Middle Atmosphere", D. Reidel Publishing Co., Dordrecht, Holland, 1995

Collins, R. L., Hallinan, T. J., Smith, R. W., Hernandez G., Lidar Observations of a Large High-Altitude Sporadic Na Layer During Active Aurora, Geophysical Research Letters, 23, 1996.

Cotton, A. F., Wilkinson, G. F.R.S., Advanced Inorganic Chemistry: A Comprehensive Text, John Wiley and Sons, New York, 1967

Cutler, L. J., Rayleigh Lidar Studies of the Arctic Middle Atmosphere, M.S. Thesis, University of Alaska, Fairbanks, 2000

Cutler, L. J., Collins, R. L., Mizutani, K., Itabe, T., Rayleigh Lidar Observations of Mesospheric Inversion Layers at Poker Flat, Alaska (65° N, 147° W), Geophysical Research Letters, 28, 8, 1467-1470, 2001

Demtröder, Wolfgang, Laser Spectroscopy: Basic Concepts and Instrumentation, Springer-Verlag, Germany, 1996

Fricke, K. H., U. von Zahn, Mesopause Temperatures Derived from Probing the Hyperfine Structure of the D_2 Resonance Line of Sodium by Lidar, Journal of Atmospheric and Terrestrial Physics, 47, 5, 499-512, 1985

Fuhr, J. R., Martin, G. A., Wiese, W. L., Atomic Transition Probabilities: Iron Through Nickel, National Measurement Laboratory, National Bureau of Standards, Maryland, 1988

Gelbwachs, J. A., Iron Boltzmann Factor LIDAR: proposed new remote sensing technique for mesospheric temperature, Applied Optics, 33, 30, 7151-7156, 1994

Granier, C., Jegou, J. P., Megie, G., Iron Atoms and Metallic Species in the Earth's Upper Atmosphere, Geophysical Research Letters, 16, 3, 243-246, 1989

Hecht, J., The Laser Guidebook, McGraw Hill, New York, 1992

Helmer, M., Plane, J. M. C., A Model of Meteoric Iron in the Upper Atmosphere, Journal of Geophysical Research, 103, D9, 10,913-10,925, 1998

Herzberg, G., Atomic Spectra and Atomic Structure, Dover Publications, New York, 1944

Hughes, D. W., Cosmic Dust, Wiley, New York, 1978

Kane, T. J., Gardner, C. S., Lidar Observations of the Meteoric Deposition of Meteoric Metals, Science, 259, 5099, 1297-1300, 1993

Kane, T. J., Gardner, C. S., Structure and Seasonal Variability of the Nighttime Mesospheric Fe Layer at Midlatitudes, Journal of Geophysical Research, 98, D9, 16,875-16,886, 1993

Kane, T. J., Mui, P. H., Gardner, C. S., Evidence for Substantial Seasonal Variations in the Structure of the Mesospheric Fe Layer, Geophysical Research Letters, 19, 4, 405-408, 1992

Kuhn, K., Laser Engineering, Prentice Hall, New Jersey, 1998

Liu, C. H., World Ionosphere Thermosphere Study, ICSU SCOSTEP, 1989

Measures, Raymond M., Laser Remote Sensing: Fundamentals and Applications, Krieger Publishing Co., Florida, 1992

Mizutani, K. Itabe, T., Yasui, M., Aoki, T., Murayama, Y., Collins, R.L., Rayleigh and Rayleigh Doppler Lidars for the Observations of the Arctic Middle Atmosphere, IEICE Transactions on Communications, E83-B, 9, 2004-2009, 2000

Plane, J. M. C., The Chemistry of Meteoric Metals in the Earth's Upper Atmosphere, International Reviews in Physical Chemistry, 10, 1, 55-106, 1991

Plane, J. M. C., Cox, R. M., Mesospheric Na Layer at Extreme High Latitudes in Summer, Journal of Geophysical Research, 103, D6, 6381-6389, 1998

Ramaswamy, V., Chanin M.-L., Angell, J., Barnett, J., Gaffen, D., Gelman, M., Keckhut, P., Koshelkov, Y., Labitzke, K., Lin, J.-J. R., O'Neill, A., Nash, J., Randel, W., Rood, R., Shrine, K., Shiotani, M., Swinbank, R., Stratospheric Temperature Trends: Observations and Model Simulations, 39, 1, 71-122, 2001

Senft, D. C., Papen, G. C., Gardner, C. S., Seasonal Variations of the Thermal Structure of the Mesopause region at Urbana, IL (40° N, 88° W) and Ft. Collins, CO (41° N 105° W), Geophysical Research Letters, 21, 9, 821-824 1994

Silfvast, William T., Laser Fundamentals, Cambridge University Press, New York, 1996

Solomon, S., Stratospheric Ozone Depletion: A Review of Concepts and History, Reviews of Geophysics, 37, 3, 275-316, 1999

Thomas, G. E., Mesospheric Clouds and the Physics of the Mesopause Region, Reviews of Geophysics, 29, 553-575, 1991

Verdeyen, Joseph T., Laser Electronics, Prentice Hall, New Jersey, 1981

von Zahn, U., $NaHCO_3$: A Source of Na Atoms for Sudden Layers?, Geophysical Research Letters, 17, 2, 147-149, 1990

Wallace, John M., Hobbs, Peter V., Atmospheric Science: An Introductory Review, Academic Press, San Diego, 1977

Wayne, R. P., "Chemistry of Atmospheres", Oxford University Press, New York, NY, 1985

Wiese W. L., Smith, M. W., Miles, B. M., Atomic Transition Probabilities: Sodium Through Calcium, National Measurement Laboratory, National Bureau of Standards, Maryland, 1969